COMPUTATIONALLY EFFICIENT SUPER RESOLUTION ALGORITHM

by

Raunaq Singh Kainth

Submitted in partial fulfilment of the requirements
for the degree of Master of Applied Science

at

Dalhousie University
Halifax, Nova Scotia
April 2016

Dedicated to my family, friends and to the memory of my grandmother

Table of Contents

List of Tables

List of Figures

ABSTRACT

Super resolution image can be obtained from combining several low resolution noisy and blurred images. We propose an efficient algorithm to produce super resolution microscopic images. In the proposed algorithm, accurate sub-pixel motion between images is essential for reconstructing the image. Denoising is carried initially by adjusting the low resolution images. Shift fusion approach is applied to enhance the resolution of image and improved optical flow method is used for registration of images. The proposed method is applied to each color channel separately. The results are tested with synthetic downgraded images, popular low resolution datasets and experimental real-life images showing significant improvement in quality of images, with considerable less time cost and memory consumption than those of existing methods. Qualitative analysis is studied through edge detection method and observing visible features. Quantitative analysis is inspected showing improvement in resolution by measuring observable minimum distance.

List of Symbols Used

2D	Two Dimensional
3D	Three Dimensional
λ	Wavelength
LR	Low Resolution
SR	Super Resolution
HR	High Resolution
F	Fourier Transform
M	Rows in matrix
N	Columns in matrix
MSE	Mean Squared Error
PSNR	Peak Signal to Noise Ratio
SSIM	Structural Similarity Index Measurement
$\sum$	Summation
δ	Shift in signal
DFT	Discrete Fourier Transform
FFT	Fast Fourier Transform
MAX_f	Maximum signal value
PFFC	Pseudo Flat Field Correction
CBC	Complete Blood Count
RBC	Red Blood Cells
WBC	White Blood Cells
l(x,y)	Luminance in an image
S(x,y)	Structural index
μ_x	Original image
μ_y	Distorted image
$\circledast$	Convolution

ACKNOWLEDGEMENTS

I would like to thank my supervisor Dr. Michael Cada for accepting me as his graduate student. His expertise, understanding and patience added considerably to my graduate school experience. I would like to thank Dr. Alan Fine for providing me an opportunity to work on this exciting project. His guidance, caring and valuable insights provided an excellent atmosphere to do research. I would also like to thank Dr. Kamal El-Sankary and Dr. William Phillips for being part of examining committee and for their support whenever required.

I also would like to thank lab members at Photonics group for productive discussion and constant support. I appreciate encouragement from Mohammed Eldio through the course of my research. Also, thanks to members of Physiology and Biophysics lab for providing a friendly environment. Support from Applied Science in Photonics and Innovative Research and Engineering, a program under Collaborative Research and Training Experience (CREATE) program funded by Natural Sciences and Engineering Research Council (NSERC) of Canada, is also acknowledged.

Finally, I would like to thank my parents, brother and sister for their constant support and encouragement.

Halifax, NS Raunaq Singh Kainth

April 1, 2016

Chapter 1 Introduction

1.1 Preface

This thesis focuses on fast super resolution image reconstruction from a series of low resolution microscopic images. The prefix “super” comes from Latin and means “above” or “beyond” [1]. Super-resolution is used to describe techniques that enhance the resolution of the resultant image through several low resolution images. Each low resolution image can be obtained from the same source but has new information present in form of subpixel shifts which are fused together by accessing relevant information from these shifts to reconstruct an image having higher resolution than the input image. Lukosz was the first to realize that spatial resolution can be gained from temporal bandwidth [2].

Multiframe super resolution has been studied extensively over the past few years. There are still challenges which exist while performing super resolution. One of them is time complexity when dealing with real time data. There are many super resolution methods proposed [2-6] and studied which relies correct registration of images and deblurring. They also rely upon on known blur kernel and level of noise in the image sequences. Many real world applications need a fast super resolution method which can perform the task quickly. The applications are in space technology, medical field, surveillance cameras, forensic and satellite imaging. One of the applications this thesis focuses is on medical technology for blood analysis. It should be noted that in this work new algorithm for super resolution is implemented, but due to the technology propriatery rights; part of this implementation is not shown in detail. On the other hand, a publication was accepted in a conference from this thesis.

The task is challenging because there are many unknown parameters involved. There is unknown noise in sensor, optical blur, varying illumination and camera features for each frame. We propose a complete working super resolution method with the models described in chapter 3 and 4 and results presented in chapter 5.

1.2 Motivation

Setup of high resolution imaging is expensive and there are limitations of sensor and optical devices, so that high resolution images are not always available. This constraint may be overcome by image processing algorithms giving rise to super resolution which is the focus of this thesis. In biomedical applications, there is need of simple-to-use but accurate devices. A portable hematology system offers opportunities for people to have access to valuable diagnostic analysis, anywhere in the world. This could be done using low resolution images which can be combined together to achieve a desirable high resolution for analysis.

Many super resolution algorithms produce high detail image but lacks in the computational complexity needed for large volume of image datasets. Combining the numerous advantageous, pragmatic applications and possibilities this algorithm can accomplish and challenges on making it computationally inexpensive at the same time producing a high quality result has excited us to work on this research. This book presents the process of obtaining a super resolved image which is accurate enough onto which blood cells classification and other analysis can be performed.

1.3 Objectives

1. To design a complete and computationally efficient super resolution algorithm reconstructing a high resolution image for doing complete blood count.
2. To design a motion estimation algorithm which accurately determines subpixel shift between the captured low resolution images, independent of hard configuration of optical device.
3. To use a benchmark for image quality for testing simulated images and experimental images.
4. To quantitatively analyze the reconstructed results expressing the minimum distance resolved between the two objects.

1.4 Outline of Thesis

The chapters in the book are organized as follows. In chapter 2, the theory behind super resolution is described with previous works done in this area in the past. The criteria used behind the assessment of quality images are also discussed. Chapter 3 provides the improved method used for motion estimation and analysis of performance. In chapter 4, the proposed super resolution method is explained in detail outlining various steps involved. Chapter 5 gives thorough analysis of results through various image quality parameters. These are categorized into three sections, which are: standard test images, simulated images and experimental dataset. Quantitative analysis for simulated and several experiments is shown. Time complexity is also discussed by our suggested method. Chapter 6 concludes with our interpretations, reviews primary contributions and remarks for possibility of future research.

Chapter 2 Background Theory

2.1 Super Resolution

In today's world, images with high resolution are desirable and sometimes need as a requirement for critical applications [1]. High resolution images provide more details; have less noise and more pixel density but common imaging systems have limits during image acquisition as shown in Figure 2.1 which contains optical distortion, spatial aliasing, motion blur and noise in the system. Figure 2.2 provides connection between 4 low resolution samples and high resolution image.

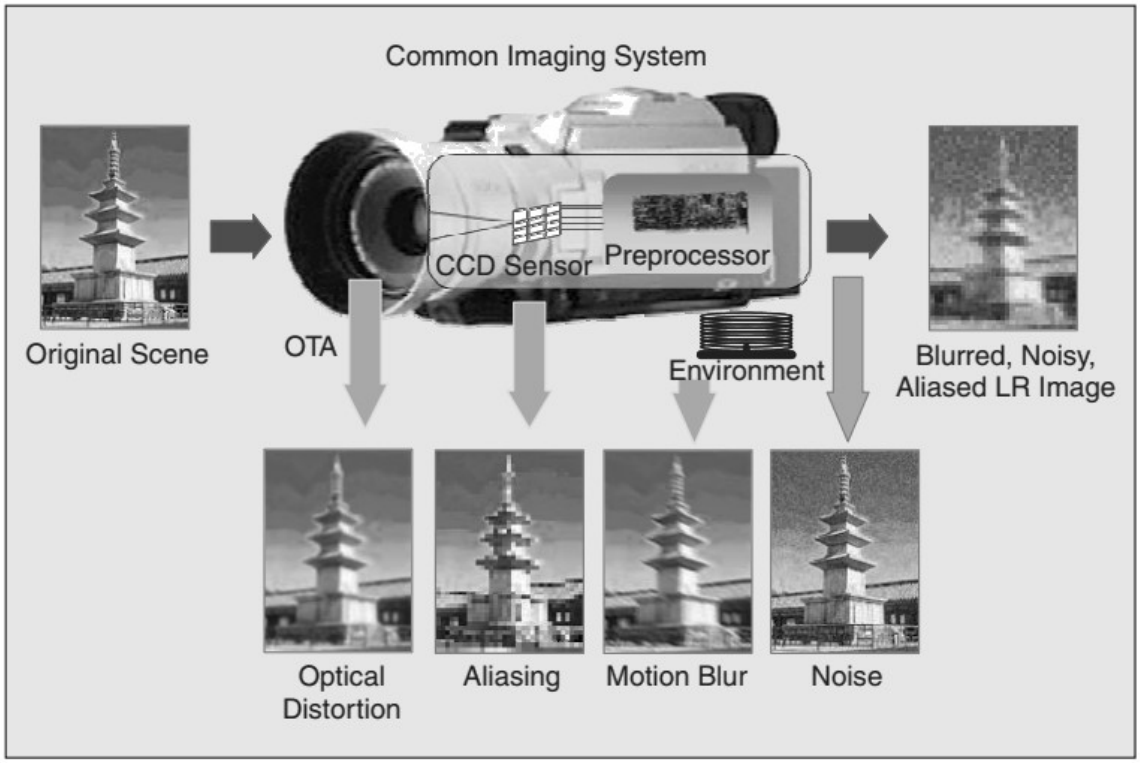

Figure 2.1 Common Imaging System [7]

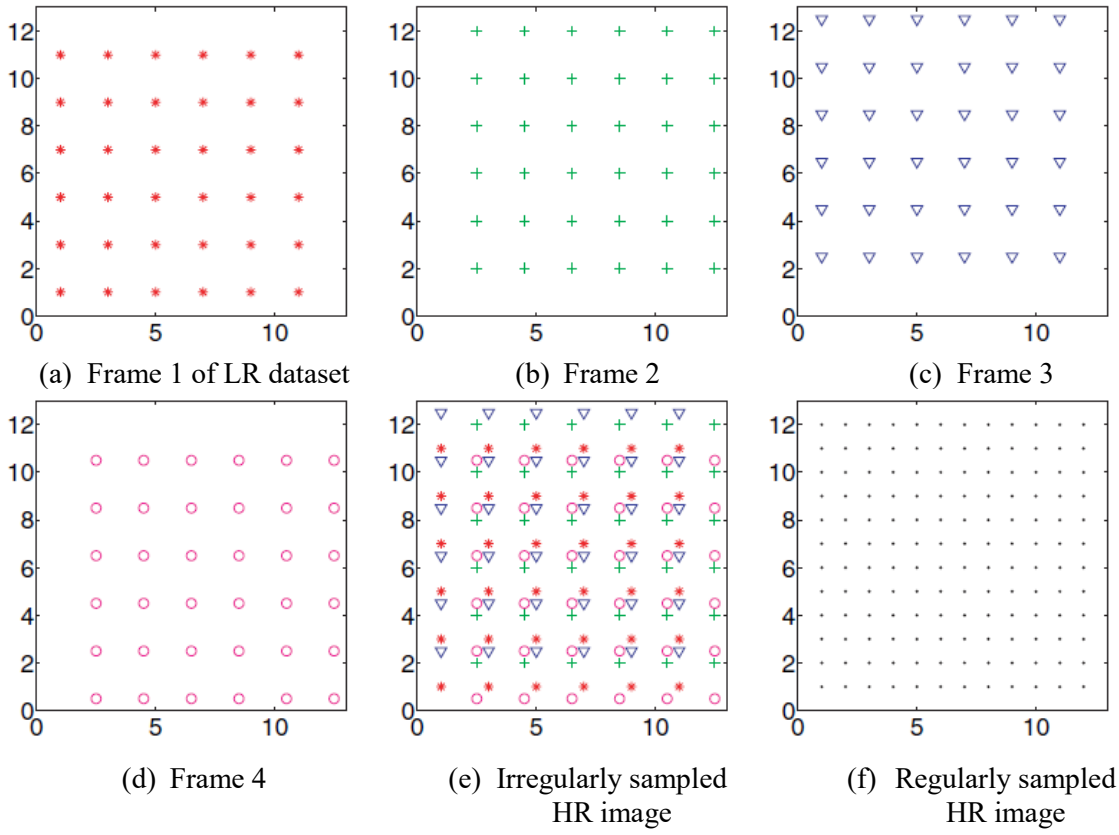

(a) Frame 1 of LR dataset (b) Frame 2 (c) Frame 3

(d) Frame 4 (e) Irregularly sampled HR image (f) Regularly sampled HR image

Figure 2.2 Relationship between LR and HR images [8]

The super resolution is possible when Nyquist criterion is satisfied as LR observed image represents aliased version of the original image. The observed images can be combined to remove aliasing producing higher resolution image. Description about possibility of super resolution is as follows [9][10]

Consider a 1D signal, free from blur or noise. If this signal is continuous with p kinds shifted by amount δ_k, where $k = 0,1,2 \ldots\ldots p-1$, then

$$f_k(x) = f(x + \delta_k) \tag{2.1}$$

A sampled version of f_k, for $n = 0,1,2 \ldots\ldots N-1$, will be,

$$f_{kn} = f(nT + \delta_k) \tag{2.2}$$

where, T is the sampling period.

Let, $F_k(\omega)$ and $F(\omega)$ be the Fourier transform of $f_k(x)$ and $f(x)$, respectively.

The continuous Fourier transform of equation (2.1) is,

$$F_k(\omega) = e^{i2\pi\delta_k\omega}F(\omega) \tag{2.3}$$

Let, F_{kl} be the N-point discrete Fourier transform (DFT) of kth sampled image f_{kn},

$$F_{kl} = \sum_{n=0}^{N-1} f_{kn} \exp\left(-j2\pi\frac{ln}{N}\right),\ l = 0,1,2 \dots, N-1 \tag{2.4}$$

We can relate Fourier Transform of $f_k(x)$ and discrete Fourier transform of its sampled version by sampling theorem [11], that is,

$$F_{kl} = \frac{1}{T}\sum_{m=-\infty}^{\infty} F_k\left(\frac{l}{NT} + m\frac{1}{T}\right) \tag{2.5}$$

where, $l = 0,1,2 \dots N-1$

$$F_{kl} = \frac{1}{T}\sum_{m=-\infty}^{\infty} e^{j2\pi\delta_k\left(\frac{l}{NT}+m\frac{1}{T}\right)}F_k\left(\frac{l}{NT} + m\frac{1}{T}\right) \tag{2.6}$$

Since f is bandlimited and sampling period given as T, sampling period $\omega_s = 1/T$, and L being integer, the values in the frequency spectrum can be calculated at $-L\omega_s$, $-L\omega_s + \frac{1}{NT}$,…, $-L\omega_s - \frac{1}{NT}$ which results in an enhancement of $2L$ times in resolution.

$$F(\omega) = 0\ for\ |(\omega)| \geq L/T \tag{2.7}$$

In order to avoid aliasing we should have sampled with $T' = T/2L$. From above equation (2.6), each F_{kn}, can be expressed as combination of $2L$ samples of $F(\omega)$. There are set of $p \times N$ linear equations and $2L \times N$ unknown. It can be solved if $\geq 2L$. The $2L \times N$ calculated samples of $F(\omega)$ can now be used to estimate $f(x)$from $x =$

$0, \ldots, (N-1)T$, with spacing $T/2L$. Using $k = 0$ and replacing N by $2LN$ and T by $T/2L$ in above equation the resolution can be increased by a factor of $2L$. This is the simple case for theoretical explanation. There are other factors such as blur and noise which should be taken into account.

2.1.1 Previous Works

Reconstruction of super resolution image is a restoration of image. The super resolution problems in the past years are solved in frequency domain and spatial domain. Extrapolation techniques using prolate spheroidal wave functions have been proposed by Slepian and Pollak[12]. Papolous and Gerchberg used extrapolation by error energy reduction [13][14]. The initial work to produce a super resolution image through many downsampled low resolution frames was done by Tsai and Huang [15]. They considered m low resolution frames with shift s_k. These frames are $\{f_k\}_{k=1,2\ldots m}$. If $f(x)$ is the ideal continuous image and then f_k are the samples from $f(x + s_k)$. The continuous Fourier transform of these samples is,

$$F_k(\omega) = e^{is_k\omega} F_{(\omega)} \tag{2.8}$$

The discrete Fourier transform of the samples is,

$$F_k = (\exp(-i2\pi \frac{jn}{N}))_{j,n} f_k \tag{2.9}$$

Using relationship between continuous Fourier Transform and discrete Fourier transform, given T as temporal spacing between samples, ω_s as sampling frequency of each low resolution frames.

$$F_{kn} = \frac{1}{T} \sum_{p=-\infty}^{\infty} F_k(\frac{n}{NT} + p\omega_s) \tag{2.10}$$

They calculated the values in the frequency spectrum. Kim et al discuss a recursive algorithm, also in the frequency domain, for the restoration of super-resolution images from noisy and blurred observations [16].

Projection onto convex sets (POCS) method was done by Sauer and Allebach [17] as an interpolation problem for non-uniform data. Ur and Gross [18] use the Papoulis generalized multichannel sampling theorem [19][20] to obtain an improved resolution picture from interpolation values. Blur in the images with restoration during reconstruction was considered by Irani and Peleg using iterative back projection algorithm [21]. Structure adaptive normalized convolution was formulated in [22] but is computationally expensive algorithm. Tikhnonov regularization was proposed in [23] and addressed the issue of under determined cases. Farsiu et. al incorporated regularization by estimating a blurred image with L1 norm minimization in regularization and measurement terms, they used total variation bilateral filter as deblurring function [3] which works very well for small size of the datasets but it takes lot of time to produce higher resolution image as the size of the low resolution increases. Several papers have considered super resolution from a single image [24-26] but are limited to small increase in resolution (sometimes by factors smaller than 2). Super resolution through training a set of images by learning correspondence through a database between the patches of low resolution and high resolution images was given in [27] but are unable to deliver high resolution image if blur in the images is varied. Compressed sensing approach through sparsity of patches of low resolution images was addressed in [28] and based on single image by [25]. Modelling high resolution image as Maximum a posteriori-Markov Random Field (MAP-MRF) framework and solving using graph cut optimization was investigated in [26-29], but they suffer high computational complexity for large image size. Gunturk et al proposed a Bayesian approach for the super-resolution of MPEG-compressed video sequence considering both the quantization noise and the additive noise [30] but require significant time and space complexity for processing the images. Our method overcomes these difficulties by providing an efficient approach.

2.1.2 Diffraction Limit

The resolution of an optical microscope is defined as the shortest distance between two points on a sample that can be distinguished by the observer or camera system as separate objects. The resolution of optical imaging instruments, for example, telescopes and microscopes is limited by diffraction of light which was proposed by a German physicist Ernst Abbe in 1873 [31]. The Abbe criterion is defined as:

$$r = \frac{0.5\lambda}{NA} = \frac{0.5\lambda}{n\sin(\theta)} \tag{2.18}$$

NA is the numerical aperture of the objective lens, r is the distance between two objects from each other. λ is the wavelength of the light, n is the diffraction between objective and the sample. The resolution is limited through other criterions such as the Rayleigh criterion which is described mathematically as:

$$r = \frac{0.61\lambda}{NA} = \frac{0.61\lambda}{n\sin(\theta)} \tag{2.19}$$

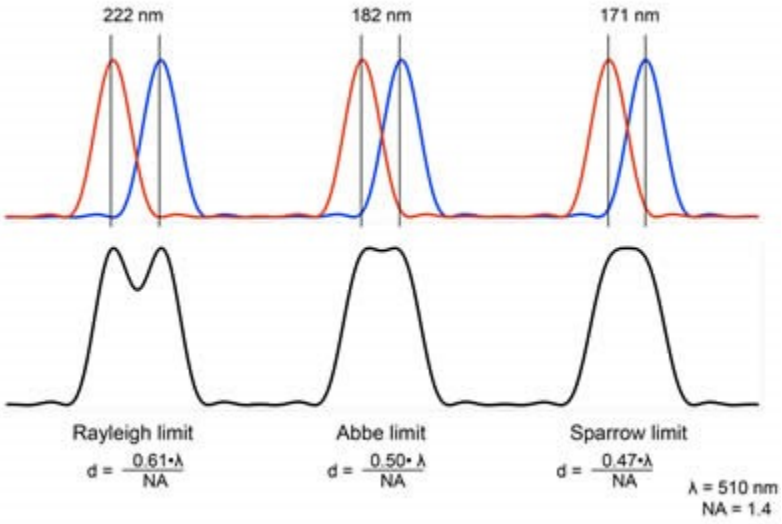

Figure 2.3 Conventional resolution limits: Rayleigh limit, Abbe limit and Sparrow limit [32]

2.1.3 Point Spread Function

The diffraction limit is caused due to the wave nature of the light and the influence with the optical system which can be diffraction, scattering at the point of contact. Point Spread Function (PSF) describes the response of the imaging system to the point source, which is basically the impulse response of the system. In spatial domain it is also transfer function of the system. Resolution depends on the wavelength of light and Numerical Aperture (NA) which is collecting ability of the objective lens.

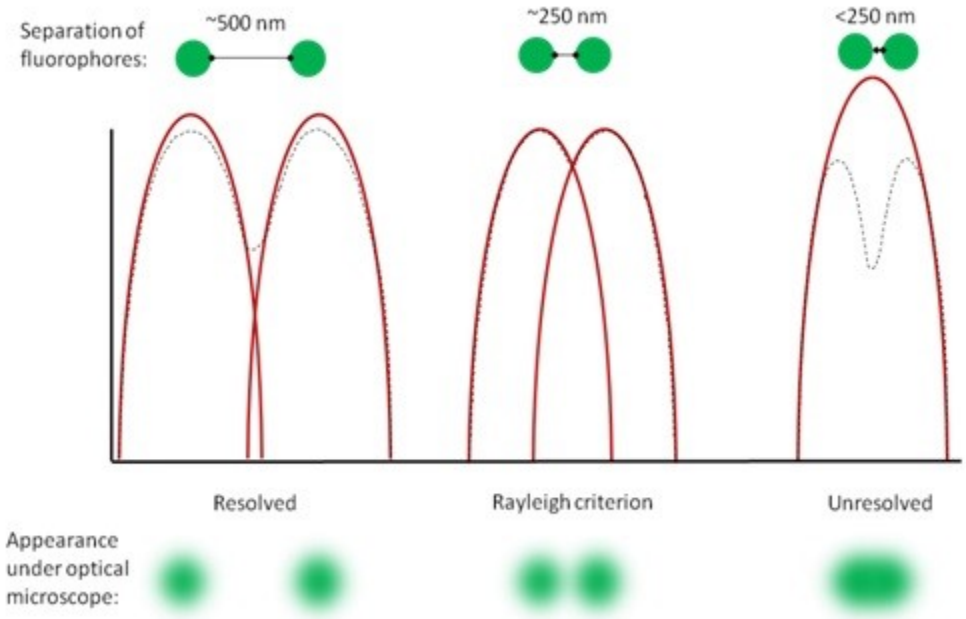

Figure 2.4 Resolution limit and ability to differentiate between point sources [33]

An image is a convolution of the object and the PSF function

$$Image = Object \circledast PSF \tag{2.20}$$

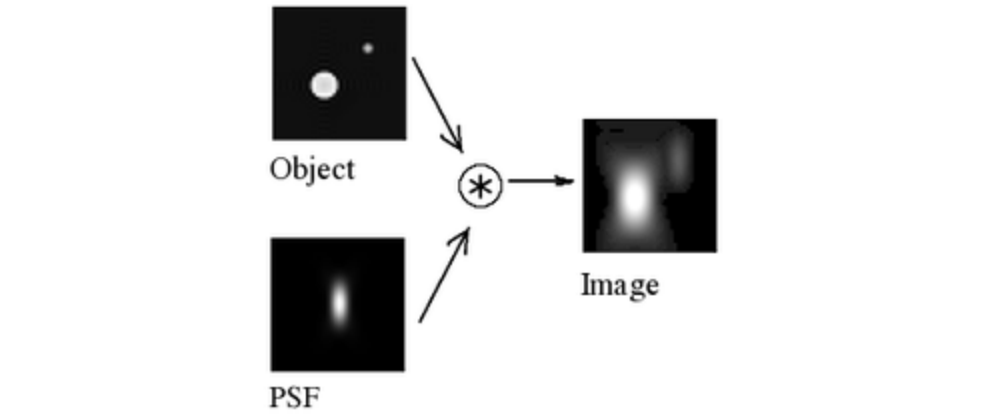

(a)

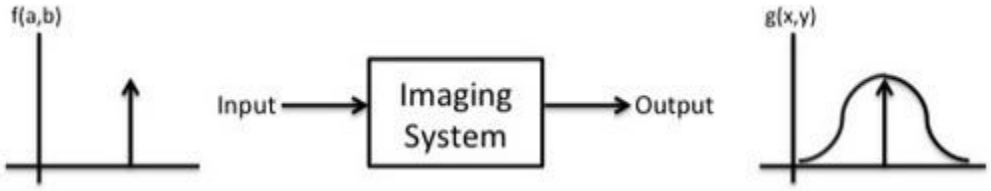

(b)

Figure 2.5 Blurring due to an imaging system [34]

The image of a point source is blurred and degraded by noise of the imaging system. If the imaging system is linear, the image of an object can be expressed as:

$$g(x,y) = \iint_{-\infty}^{\infty} h(x,y;\alpha,\beta) f(\alpha,\beta)\, d\alpha\, d\beta + \eta(x,y) \qquad (2.21)$$

Where, $\eta(x,y)$ is the additive noise function, $f(\alpha,\beta)$ is the object, $g(x,y)$ is the image, and $h(x,y;\alpha,\beta)$ is the point spread function. The ";" is used to describe the input and output pairs of the coordinates in this scenario. The point spread function (PSF) describes the imaging system response to a point input, and is analogous to the impulse response. A point input, represented as a single pixel in the "ideal" image, will be reproduced as something other than a single pixel in the "real" image.

The output image is regarded as two dimensional convolution of the ideal image. The PSF describes the imaging system response to a point input and is analogous to the impulse response.

2.1.4 Optical Transfer Function

Modulation Transfer function is a quantity used to characterize the performance of an optical system, photonic system, film scanners and video cameras. This is the system`s ability to transfer contrast to image plane at a particular resolution.

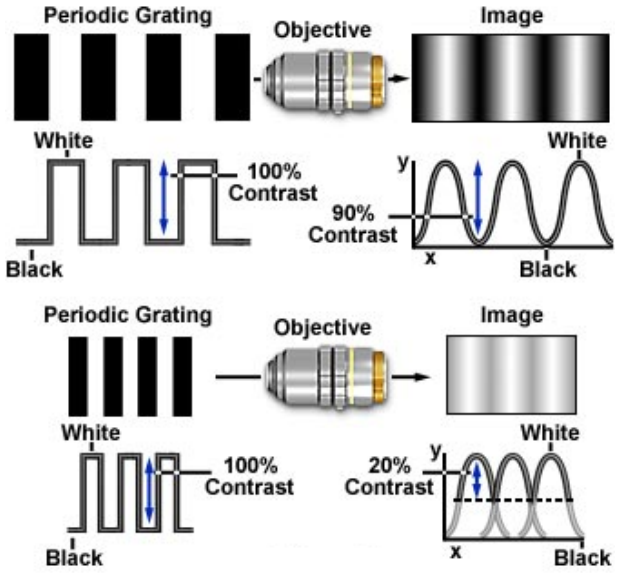

Figure 2.6 Modulation and Contrast Transfer functions [35]

MTF and OTF are related by,

$$OTF = MTF \times e^{i\varphi(f)} \tag{2.22}$$

Optical Transfer Function is conventionally expressed as the normalized Fourier transform of Point Spread Function where normalization would be such that the value of at zero frequency is one. Therefore, the optical transfer function is a spatial frequency-dependent complex variable whose modulus is the modulation transfer function, and whose phase is described by the phase transfer function.

A perfect optical system will have a unity modulation transfer function at all spatial frequencies. The relationship between the modulation transfer function and the point spread function for a diffraction-limited optical microscope is illustrated in Figure 2.7.

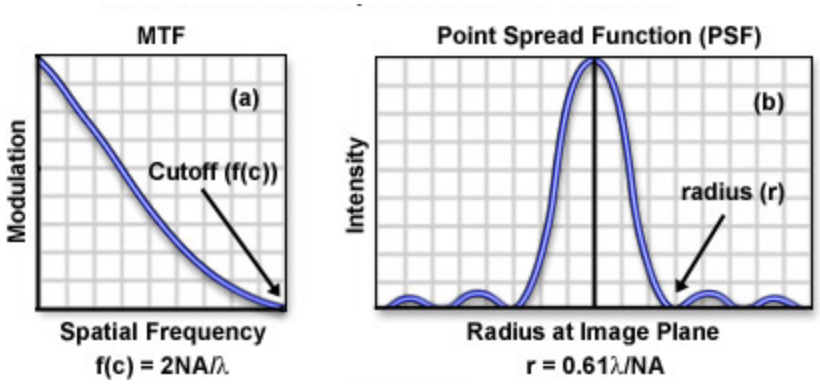

Figure 2.7 Fourier Relationship between MTF and PSF [35]

2.2 Median Filtering

Median filtering is a nonlinear method for removing noise in the image. Noise in the image is random difference of brightness or color information in the pixel values. It can be produced by sensor or circuit elements of the optical system which captures the image.

$$median[A(x) + B(x)] \neq median\,[A(x)] + median[B(x)] \tag{2.23}$$

Median filter is effective in removing noise because it preserves edges in the image which are crucial for implementing image segmentation for detecting the boundaries of the blood cells in the microscopic image.

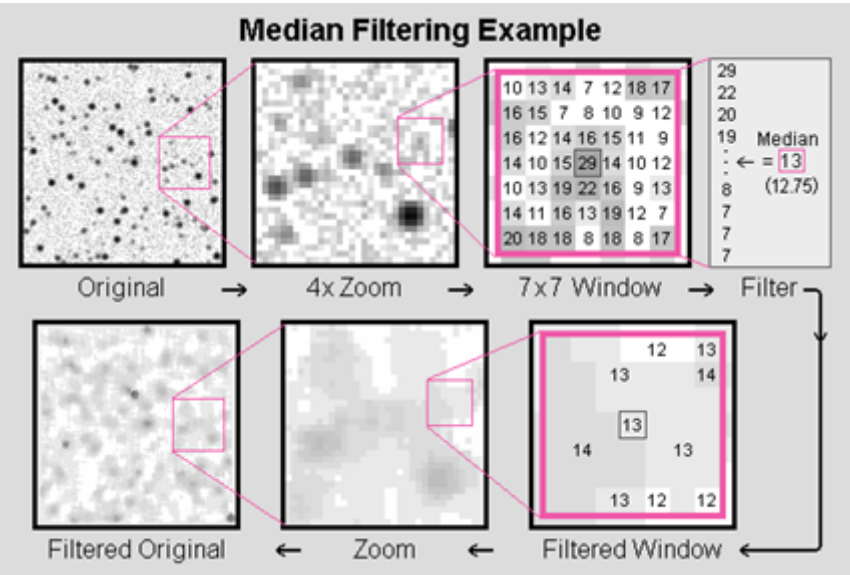

Figure 2.8 Example of Median Filtering [36]

The assumption for the neighboring pixels is that the pixel value represents the same feature as the reference pixel taking into account. In this filtering process, the pixel values in the neighbourhood window are listed according to the intensity and the middle value which is the median becomes the output value of pixel operating upon. An example of median filter operation is shown in the figure 2.9.

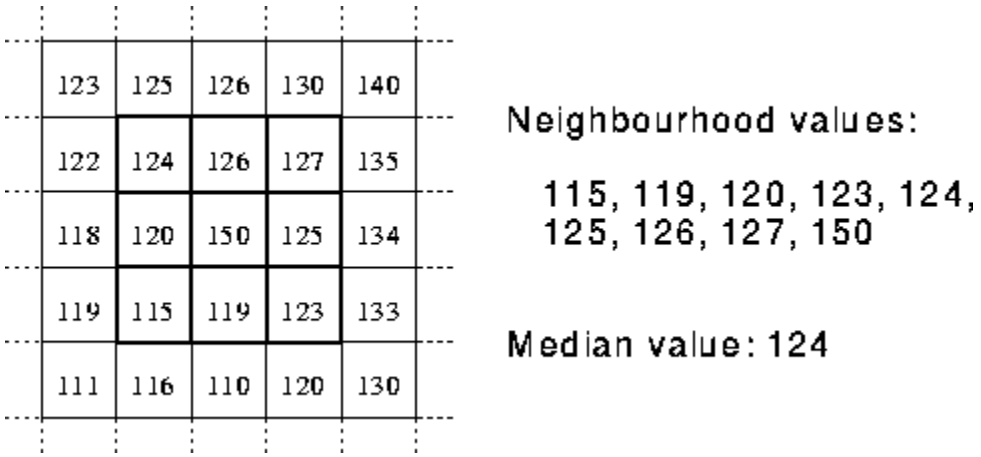

Fig. 2.9 Median filter operation for middle pixel value of 150 [37]

2.3 Assessment of Image Quality

Image enhancement or improving the visual quality of a digital image can be subjective. Quality through visual perception can vary based on different parameters used by persons. Thus, it is necessary to establish quantitative measures to compare the effects of image enhancement algorithms on image quality when the original image is available.

2.3.1 Peak Signal to Noise Ratio

Most extensively used full- reference quality measurement is peak signal to noise ratio (PSNR) and mean squared error (MSE), which is computed by averaging the squared intensity differences of low resolution and original image pixels [38]. PSNR is the ratio of power between the maximum possible value of a signal under consideration to the power of corrupted signal. It is represented on a logarithmic decibel scale.

For a standard two dimensional array of matrix, typically an image, the mathematical representation of PSNR is given as,

$$PSNR = 20log_{10}\frac{MAX_f}{\sqrt{MSE}} \tag{2.24}$$

Mean squared error (MSE), is calculated as,

$$MSE = \frac{1}{mn}\sum_{0}^{m-1}\sum_{0}^{n-1}||f(i,j) - g(i,j)||^2 \tag{2.25}$$

Here, **f** is the matrix data of our ground truth image
g is the matrix data of our degraded image in question
m are the numbers of rows of pixels of the images and i represents the index of that row
n are the number of columns of pixels of the image and j represents the index of that column
$\mathbf{MAX_f}$ is the maximum signal value that exists in original image.

The drawback of this measurement is that it relies stringently on numeric evaluation and does not essentially take into account any level of other factors of the human vision system such as the structural similarity index (SSIM).

2.3.2 Structural Similarity Index

PSNR and MSE are appealing because they are easy to calculate, have clear physical meanings, and are mathematically convenient in the context of optimization. But they are not very well matched to perceived visual quality and only rely on numerical calculations [38-41].

SSIM attempts to measure the change by three factors which are luminance, contrast and structure of the image. The results are combined and averaged to generate a final SSIM index value as shown in Figure 2.10.

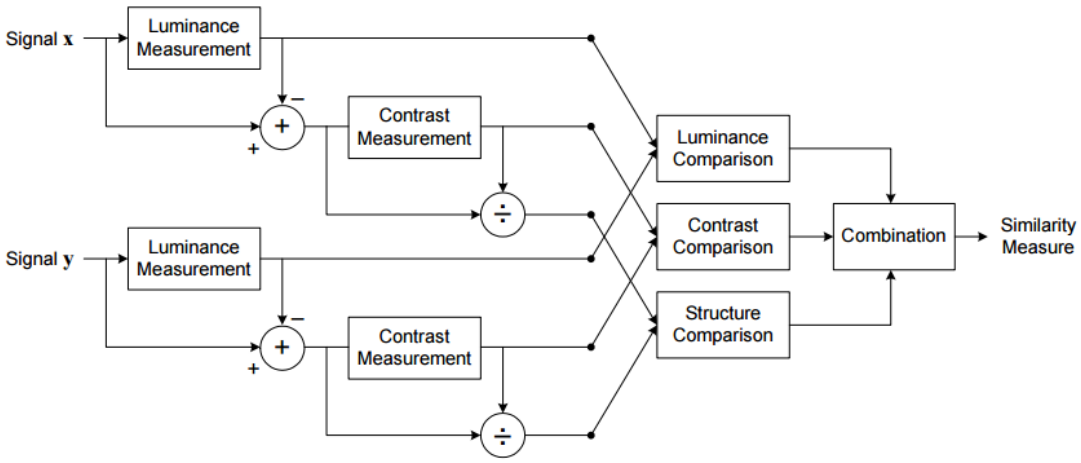

Figure 2.10 Diagram showing Structural similarity measurement system [42]

To show how SSIM is calculated [42], consider x and y are positive image signals which are aligned with each other. Constant C_1, C_2, C_3 are included to avoid instability. In grayscale image, the luminance value is the pixel value. In a color image, luminance is calculated by

$$L = 0.27\,red + 0.67\,green + 0.06\,blue \tag{2.26}$$

Let μ_y be the distorted signal and μ_x be the original signal. The luminance comparison $l(x, y)$ is function of μ_x and μ_y

$$\mu_x = \frac{1}{N}\sum_{i=1}^{N} x_i \tag{2.27}$$

The constant C_1 is defined as,

$$C_1 = (K_1 L)^2, \tag{2.28}$$

where L is the dynamic range of the pixel values (255 for $8 - bit$ grayscale images), and $K_1 \ll 1$ is a small constant.

$$l(x, y) = \frac{2\mu_x\mu_y + C_1}{\mu_x^2 + \mu_y^2 + C_1} \tag{2.29}$$

For contrast comparison $c(x, y)$, constant C_2 is given as,

$$C_2 = (K_2 L)^2, \tag{2.30}$$

where, $K_2 \ll 1$ is a small constant.

$$c(x, y) = \frac{2\sigma_x \sigma_y + C_2}{\sigma_x^2 + \sigma_y^2 + C_2} \tag{2.31}$$

Structure comparison is defined by,

$$s(x, y) = \frac{\sigma_{xy} + C_3}{\sigma_x \sigma_y + C_3} \tag{2.32}$$

Similarity measure is function of the three parameters defined above,

$$SSIM(x, y) = f(l(x, y), c(c, y), s(x, y))$$
$$SSIM(x, y) = l(x, y)^{\alpha} \cdot c(x, y)^{\beta} \cdot s(x, y)^{\gamma} \tag{2.33}$$

With setting parameters, $\alpha = 1$, $\beta = 1$, and $\gamma = 1$ and $C_3 = {}^{C_2}/_2$, the equation is derived in Appendix A1.

2.4 Image Features

Edges are local variation in the image intensity. Edges typically occur on the boundary of the regions. Edge detection has major feature for image analysis and has many application in field of morphology, computer vision research [43].

The edge of an image greatly reduces the quantity of data to be processed, and preserves essential information regarding the shapes of objects in the scene. Image segmentation is standard and fundamental problem in computer vision [44]. Edge detection methods such as the Robert edge detector, the Sobel edge detector [45] and the Canny edge detector [46] are based on variation of intensity.

We use edge detection technique to see edges of the components in the blood cells. The low resolution image edges remain undistinguishable while our reconstruction method provides sharp edges. Sobel edge detection method [44] is used to find the approximate absolute gradient magnitude which are the horizontal and vertical direction edges in an input grayscale image which is quiet useful for image segmentation. Let G_x and G_y be the convolution kernels in the vertical and horizontal directions.

Table 2.1 Vertical mask G_x for sobel edge detector

-1	0	1
-2	0	2
-1	0	1

Table 2.2 Horizontal mask G_y

-1	-2	-1
0	0	0
1	2	1

The gradient magnitude is given in (2.34) and an example of this operation is given in Figure 2.11.

$$|G| = |G_x| + |G_y| \tag{2.34}$$

(a) 8 bit Lena image

(b) Image after applying Horizontal Mask

(c) Image after applying Vertical Mask

(d) Image after calculating magnitude of the gradient.

Figure 2.11 Sobel operator example

Chapter 3 Motion Estimation

3.1 Introduction

Super resolution can be obtained when all the prerequisites are complete. One of them is presence of motion between the frames, in this case, images which are captured. Small amount of motion is necessary for reproducing high quality images because each frame contains new and different information from other frames. When the frames are captured there can be motion in any direction. This can be in vertical, horizontal or even rotational. In this thesis we are focusing on vertical and horizontal motion only.

Motion is natural property of the universe. Motion estimation is important for doing super resolution. It is essential for doing image registration which is one of the components in super resolution. It is a pre-processing step required to produce a high resolution image. It is an ill-posed problem; therefore various restraints are needed to obtain a unique and stable solution [47]. Parameters are determined from motion estimation which is global translational displacements. Accurate subpixel displacements are crucial for registration of image which directly affects the quality of reconstruction of super resolved image. It is the preprocessing step for super resolution. Subpixel details are extracted through optical flow method for each frame from the dataset. This information is used to register all these frames to a chosen reference frame. Inaccurate registration leads to noisy and misaligned reconstruction of image. The method we employ finds the estimation parameters from the image produces very good results.

In this chapter, we describe the optical flow model for raw data sets [48][49] and use the modified model for motion estimation for microscopic images. Suitable frame size of the motion is chosen for real world images instead of considering full scale image. This step is processed rapidly depending upon the number of images, which reduces computation speed by considerable amount. Pseudo flat field correction is required step to remove outliers, noise and to have constant to minimum variation brightness in the pixels. This is processed through taking a Gaussian smoothing filter and performing two dimensional convolution.

Resolution of image is enhanced by relative displacements in the image sequence and aligning them to the reference image chosen. This process of aligning is called image registration. Low resolution image suffers from geometrical transformation which is misalignment in the image because of sensor and lens distortions. Figure 3.1 shows different types of transformations on an image. We consider translational model which is the shift in 2D space. These images have to be registered to a reference frame which is also a low resolution frame which is fused together onto a high resolution empty grid.

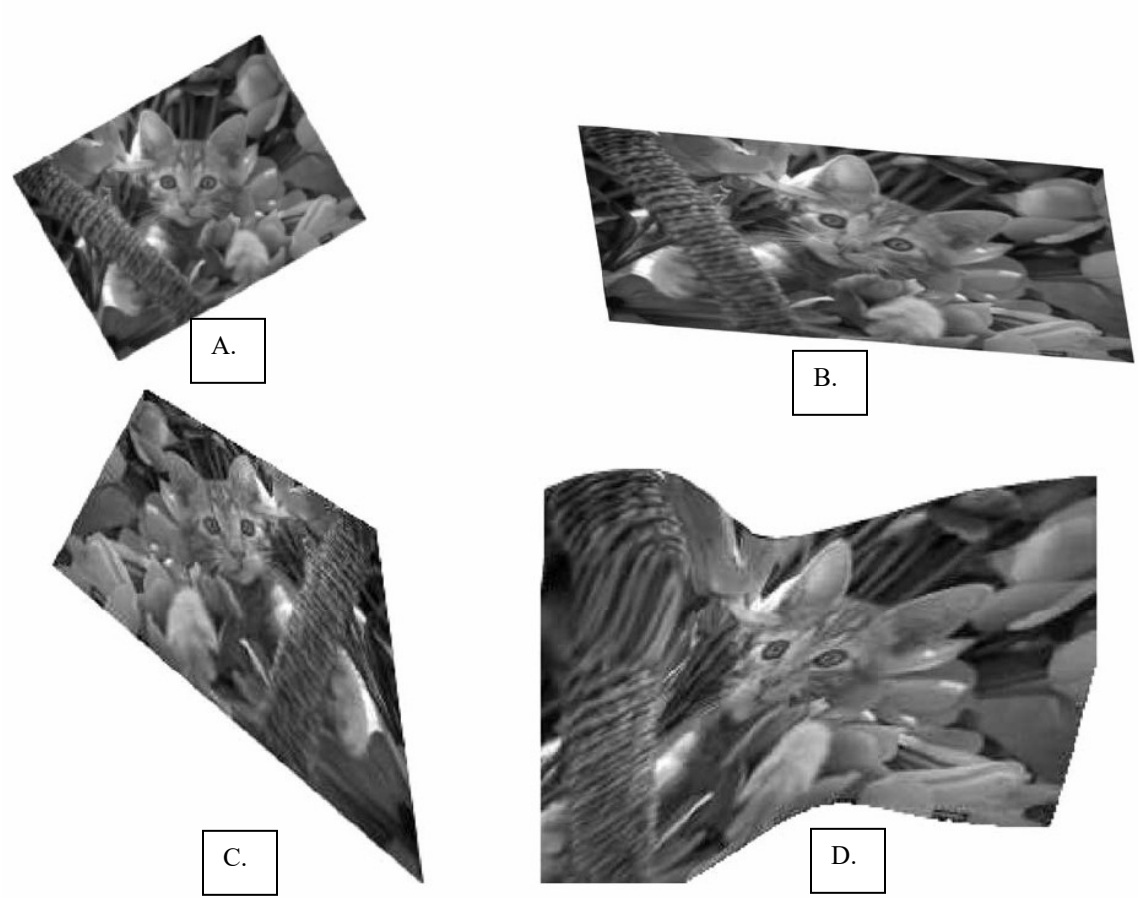

Figure 3.1 Various transformations shown above.
A. Rigid transformation involving rotation and translation; B. Affine transformation includes skew and scaling; C. Projective transformation; D. Deformable transformation

3.2 Optical Flow

Lukas Kanade proposed an algorithm for image alignment in 1981 which is widely used for various computer vision applications [50]. Optical flow is a process used to compute motion of pixels in an image sequence. It is dense image based motion estimation which relies on certain assumptions in order to compute the required parameters for super resolution algorithm. These parameters are shifts in the x and y direction in the image. When there is difference between the brightness and illumination in the scenes, in this case the microscopic image of human blood sample, the difference is observed which is the motion between the objects in the world and apparent motion.

The brightness consistency is one of the assumptions which is rather not constant in the real world scenario. There are frequent changes in the illumination in the real world scenes. As we are dealing with microscopic images which have uneven illumination in each frame, it becomes challenging to estimate the pixel movement in subpixel dimension. We solve this problem by employing the PFFC method explained later in the chapter which not only robustly gives accurate estimation for different kinds of scenes but is computationally inexpensive as well.

Motion field can be defined as the 2D projection of a 3D motion onto an image plane. Optical flow is defined as the apparent motion of the brightness pattern in the space. It is the core area of computer vision used to approximate motion. Given a sequence of images, we want to determine the movement of the objects which gives us the optical field approximation as shown in the Figure 3.2 [52]

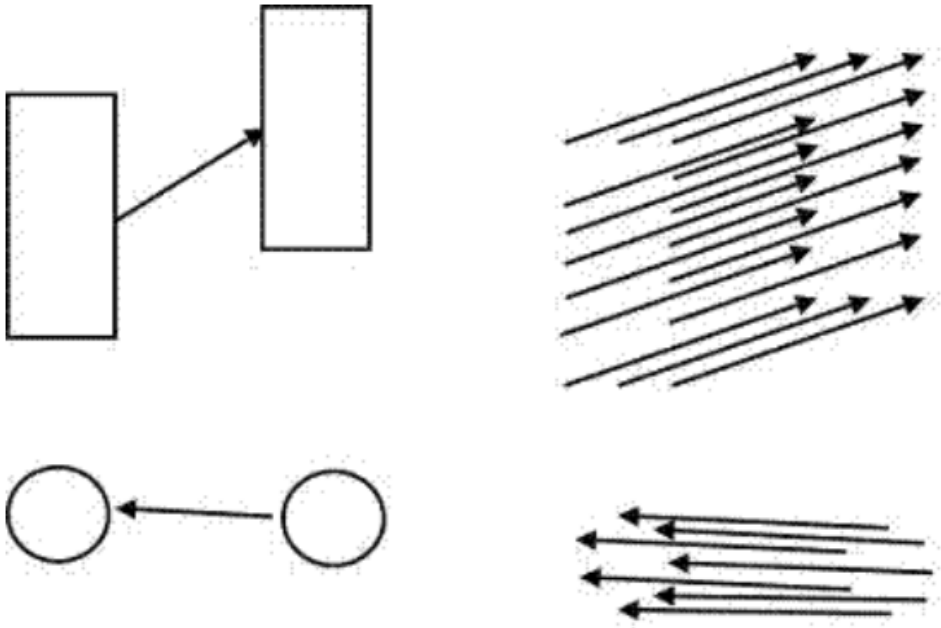

Figure 3.2 Movement of objects over two frames on the left and optical flow vectors for objects on the right

The optical flow can also be seen by a famous barberpole illusion in the following figure.

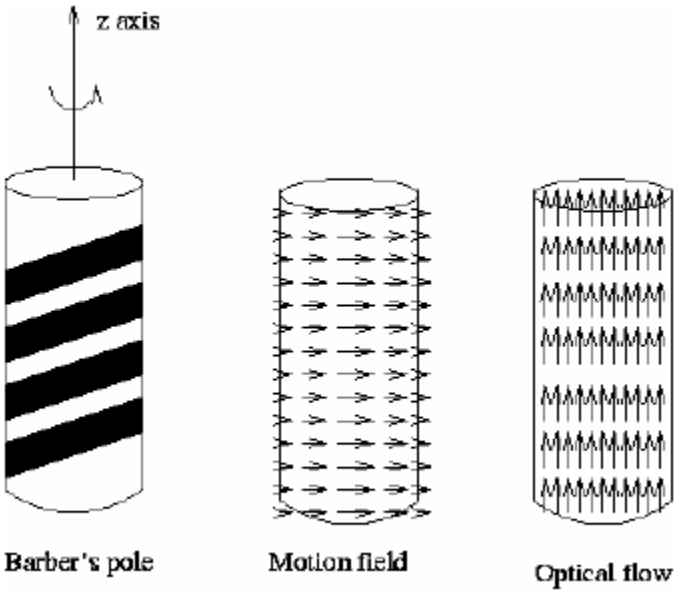

Figure 3.3 Barberpole illusion showing difference between motion field and optical flow

3.2.1 Preliminaries

In order to estimate motion through method we are using, there are some assumptions made for it to work. Here are the following assumptions –

1. Constant Brightness – The total intensity is conserved from one frame to another. The apparent brightness of moving objects remains constant. This is a rather heavy assumption as it fairly holds true under ideal conditions. Let $I(x, y, t)$ be the image intensity function in space and time. The movement of image intensity of a pixel can be represented as:

$$I(x, y, t) = I(x + u, y + v, t + 1) \tag{3.1}$$

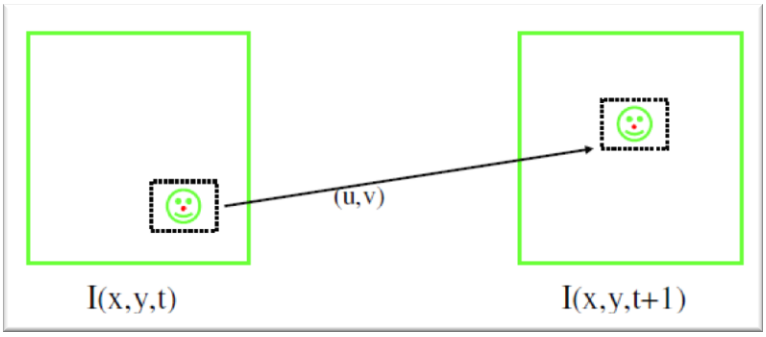

Figure 3.4 Pixel movement from one frame to another

By first order Taylor expansion of (3.1)

$$I(x(t+1), y(t+1), t+1) = I + \frac{\partial I}{\partial x}\frac{\partial x}{\partial t} + \frac{\partial I}{\partial y}\frac{\partial y}{\partial t} + \frac{\partial I}{\partial t}$$

$$= I + I_x u + I_y v + I_t \tag{3.2}$$

The linearized version of this constancy assumption yields the optical flow constraint,

$$I + I_x u + I_y v + I_t = I$$

$$I_x u + I_y v + I_t = 0 \tag{3.3}$$

There are two velocities with only one equation. We introduce another assumption of spatial coherence.

2. Spatial Coherence – The points beside each other which are neighbours, in this case – the image pixel neighbours belong to the same surface, therefore should have similar motion or more so have same velocities. If $n \times n$ is the size of the window, it solves the aperture problem [51]. But it gives us lots of equations to

solve with many unknowns, so it becomes a minimization problem. If p_n are the neighbouring pixels, we can write in matrix form:

$$\begin{bmatrix} I_x(p_1) & I_y(p_1) \\ I_x(p_2) & I_y(p_2) \\ \vdots & \vdots \\ I_x(p_n) & I_y(p_n) \end{bmatrix} \begin{bmatrix} u \\ v \end{bmatrix} = - \begin{bmatrix} I_t(p_1) \\ I_t(p_2) \\ \vdots \\ I_t(p_n) \end{bmatrix} \tag{3.4}$$

The above equation can be expressed as:

$$A\,x = b$$
$$x = (A^t A)^{-1} A^t b \tag{3.5}$$

Using iterative estimation, optical flow can be approximated as shown in the figure 3.5

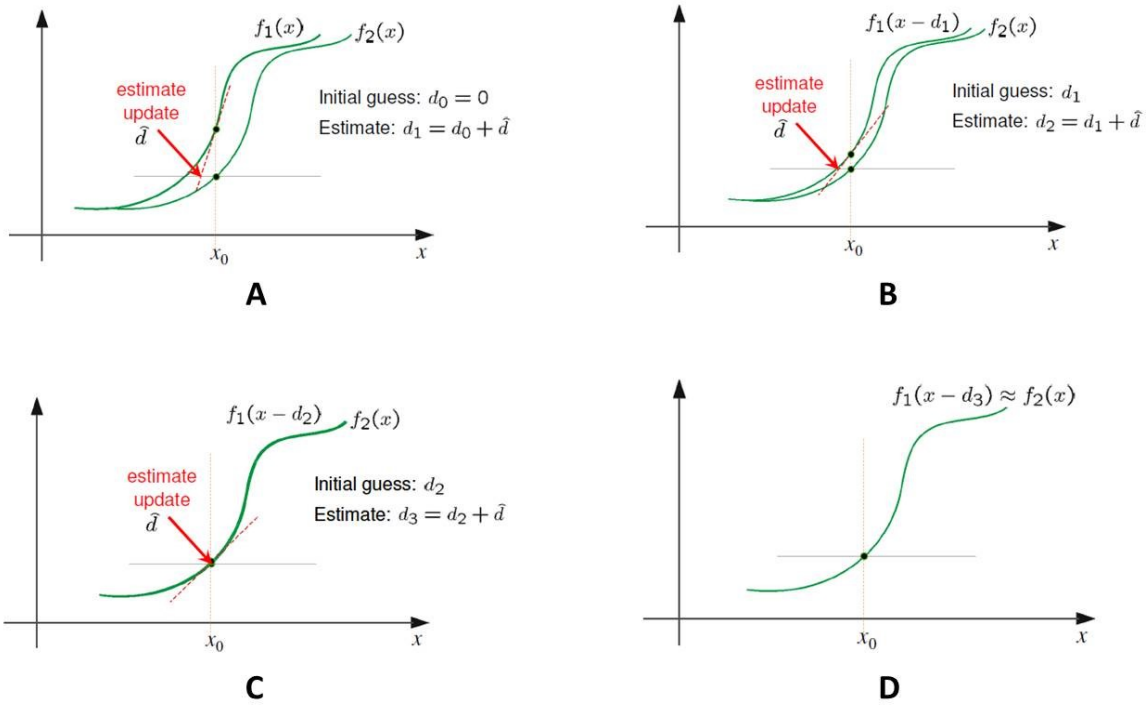

Figure 3.5 Example of 1D iterative optical flow where $f_1(x)$ is the starting function and $f_2(x)$ is the target function

In the next section, we will look into a famous optical flow method to solve these equations.

3.2.2 Lukas Kanade Algorithm

One of the popular methods for optical flow computation is Lukas and Kanade's differential method [50]. It uses weighted least squares method to approximate the optical flow relying on the assumption of spatial coherence such that the vector is similar to the surrounding pixel area and the displacement between the frames is small and approximately constant within the neighbourhood of pixel (u, v) under consideration.

Sum of squared differences can be written as:

$$\text{SSD} = \Sigma(I(x+u, y+v, t+1) - R(x, y, t))^2 \tag{3.6}$$

We aim to find (u, v) that minimizes the sum of squared differences over the region A.

$$\min_{u,v} SSD(u, v) = \min_{x,y} \sum_{x,y \epsilon A} (I_x u + I_y v + I_t)^2 \tag{3.7}$$

Optimal (u, v) which satisfies Lukas-Kanade equation given the following conditions are met for the following equation:

$$\begin{bmatrix} \Sigma I_x^2 & \Sigma I_x I_y \\ \Sigma I_x I_y & \Sigma I_y^2 \end{bmatrix} \begin{bmatrix} u \\ v \end{bmatrix} = -\begin{bmatrix} \Sigma I_x I_t \\ \Sigma I_y I_t \end{bmatrix} \tag{3.8}$$

$$A^T A \quad = \quad A^T b$$

In order to solve the equation, following conditions are to be met,

1. $A^T A$ should be invertible.
2. Eigen values λ_1 and λ_2 of $A^T A$ should not be too small.
3. ${\lambda_1}/{\lambda_2}$ should not be too large to avoid noise.

This method has an advantage over iterative method of Horn and Schunk [52] because the optical flow vector is local instead of global so we are able to find a good estimate. For each pixel, an optical flow consistent with the neighbouring spatial and temporal gradients is calculated.

Let I be the input image, R be the reference image and T be the transformation between the input and the output image. We assume that motion is very small in the amount of subpixel shift. We have,

$$0 = I(x+u, y+v) - H(x,y)$$
$$\approx I(x,y) - I_x u + I_y u - H(x,y) \tag{3.9}$$

Where, image H is warped or transformed towards I using the estimated flow field and this is repeated until convergence. For improving accuracy, iterative Lukas-Kanade algorithm is implemented by estimating the velocity at each pixel by solving the equation (3.8) using Newton-Raphson method.

Temporal Aliasing: Images having lower temporal sampling rates than required by sampling theorem to uniquely construct continuous signal causes a problem in motion estimation. This can be solved by using iterative process of creating Gaussian pyramids and calculating image derivatives at the coarsest image level.

If the motion is found to be large, we reduce the resolution of the image using Gaussian pyramids. It decomposes images into information at multiple scales to extract features and to attenuate noise. Optical flow can be estimated at coarsest scale of a Gaussian pyramid where velocities are very slow because of subsampling. As shown in Figure 3.6 and 3.7, each estimate can be used to warp the next pyramid level to stabilize the motion between the frames. This can be repeated until the optimum level of pyramid is reached.

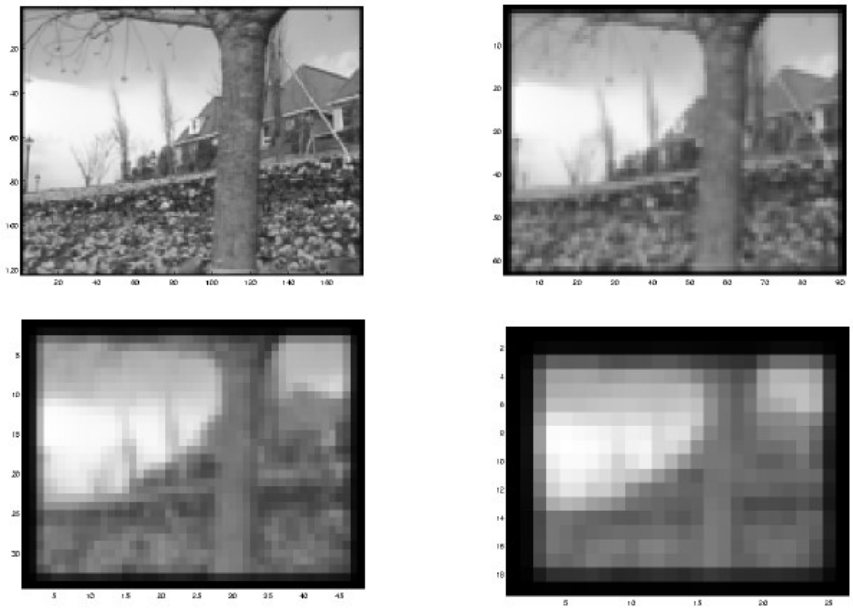

Figure 3.6 Reducing resolution if the motion is large to estimate [52]

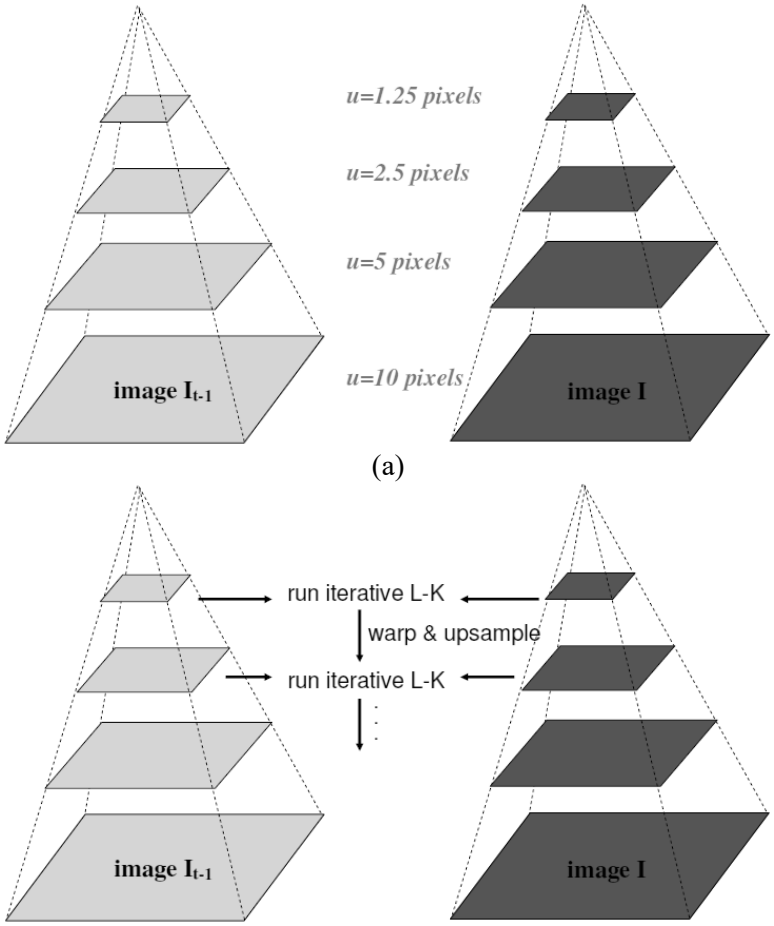

Fig 3.7 Coarse to fine optical flow motion estimation through Gaussian pyramids [52]

3.3 Pseudo Flat Field Correction

FFC are used to improve the quality of digital imaging by removing artifacts triggered due to variation of pixel intensity across the chip during image acquisition. The effects of the stationary noise patterns and variable pixel responses that commonly occur with uniform exposure of digital detectors can be effectively reduced by simple 'flat- field' image processing methods [54].

If optical method described is implemented for finding motion estimate between the microscopic frames, it would fail because it doesn't employ the uneven illumination in the equation. As the method of capturing these experimental images are designed in such a manner that it creates uneven illumination, we need a flat field image to correct the captured image, and then proceed to estimate the motion. With image processing algorithms we can generate pseudo flat field image which is very fast in speed and corrects the frames captured. This overall process is called Pseudo Flat Field Correction (PFFC).

Let's consider G the blur kernel. The FFT convolution between the image under consideration which is the input image and the blur kernel in time domain would be equivalent to multiplication in the frequency domain, according to convolution theorem. The Fourier transform between image I and kernel G can be expressed as,

$$F\{I * G\} = F\{I\} \,.\, F\{G\}$$

or,

$$f(x,y) * g(x,y) = F(u,v).G(u,v) \tag{3.10}$$

Where, $f(x,y)$ is the image in spatial domain $g(x,y)$ is the Gaussian kernel.

Discrete Fourier transform for the image can be written as,

$$F(u,v) = \frac{1}{NM}\sum_{x=0}^{N-1}\sum_{y=0}^{M-1} f(x,y)e^{-2\pi i(\frac{ux}{N}+\frac{vy}{M})} \tag{3.11}$$

Gaussian kernel with 2D distribution is expressed as,

$$g(x,y) = \frac{1}{2\pi\sigma^2}\exp(-\frac{x^2+y^2}{2\sigma^2}) \tag{3.12}$$

The discrete Fourier transform would be,

$$G(u,v) = \frac{1}{NM}\sum_{x=0}^{N-1}\sum_{y=0}^{M-1}\frac{1}{2\pi\sigma^2}e^{-\frac{x^2+y^2}{2\sigma^2}}e^{-2\pi i(\frac{ux}{N}+\frac{vy}{M})} \tag{3.13}$$

Let,

$$H(u,v) = F(u,v).G(u,v) \tag{3.14}$$

Gaussian kernel with 2D point spread function is smoothing convolution operator used to blur and reduce noise in the images. For $\sigma = 1$ with mean $(0,0)$, the Gaussian distribution is shown in the Figure 3.8.

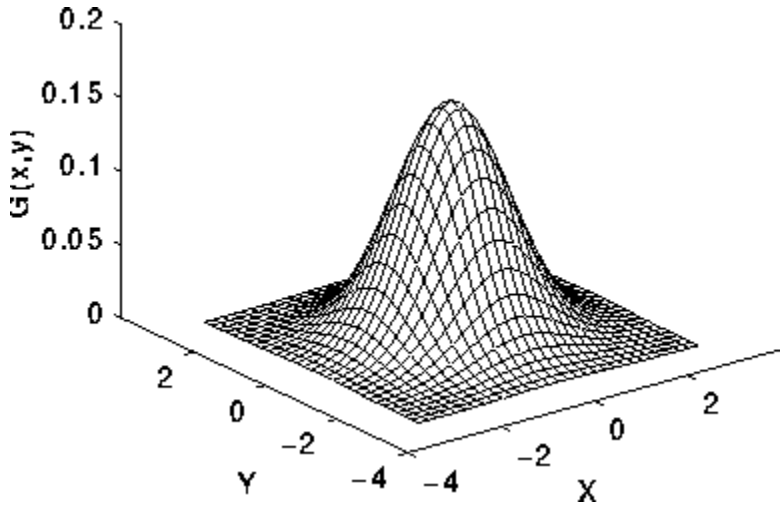

Figure 3.8 2D Gaussian distribution

Equation (3.15) gives us the pseudo flat field image which is generated for every frame. The pseudo flat field corrected image I_f is obtained by taking ratio of noisy image to the pseudo flat field image and multiplying it by mean value of pixels of the pseudo flat field image.

$$I_f = \frac{I}{\frac{1}{NM}\sum_{x=0}^{N-1}\sum_{y=0}^{M-1} H(u,v)e^{2\pi i(\frac{ux}{N}+\frac{vy}{M})}} \times \frac{\sum_{x=0}^{m}\sum_{y=0}^{n} I(x,y)}{MN} \tag{3.15}$$

Equation 3.5 is our modified equation is processed to find the motion estimation. M and N are length and breadth of matrix respectively. Optical flow equation is modified in the following form:

$$\begin{bmatrix} I_{fx}(p_1) & I_{fy}(p_1) \\ I_{fx}(p_2) & I_{fy}(p_2) \\ \vdots & \vdots \\ I_{fx}(p_n) & I_{fy}(p_n) \end{bmatrix} \begin{bmatrix} u \\ v \end{bmatrix} = - \begin{bmatrix} I_{ft}(p_1) \\ I_{ft}(p_2) \\ \vdots \\ I_{ft}(p_n) \end{bmatrix} \tag{3.16}$$

where, $I_{fx} = \frac{\partial I_f}{\partial x}$, $I_{fy} = \frac{\partial I_f}{\partial y}$ and $I_{ft} = \frac{\partial I_f}{\partial t}$

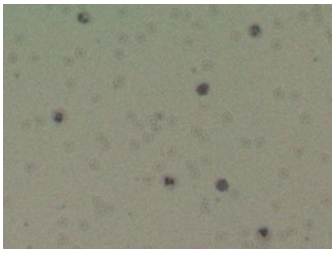

(a) RAW image, optical flow method fails to work for this image.

(b) Pseudo Flat Field image

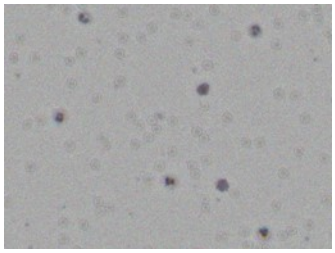

(c) Corrected image

Figure 3.9 PFFC correction

For experimental images, processing full scale image can be computationally time expensive. As there is global translation, we work with a small block with the same size and same location for each frame. The size of the block chosen is 200×200 pixels at center of the frame.

3.4 Performance Analysis

The performance of Pseudo Flat Field correction is compared with the original method and variation in the results are seen. Results obtained using our method provides better reconstruction because it takes varying pixel intensities into account.

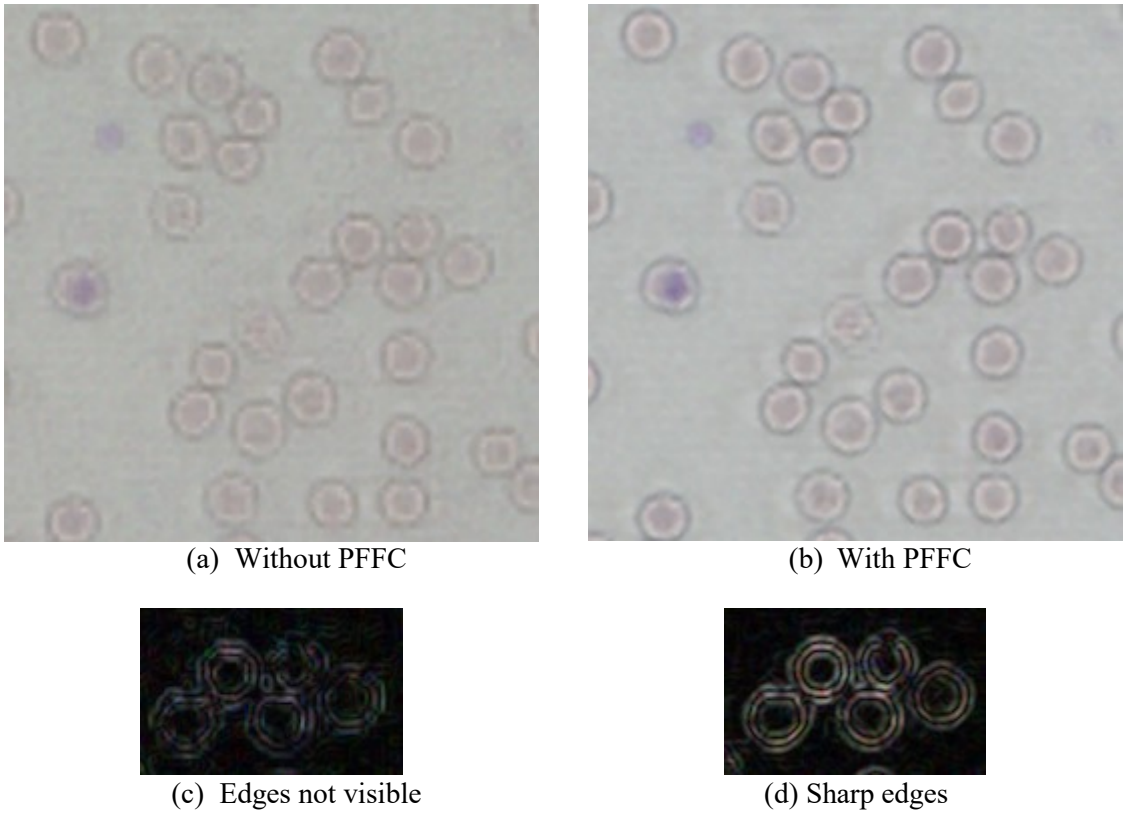

(a) Without PFFC (b) With PFFC

(c) Edges not visible (d) Sharp edges

Figure 3.10 Reconstruction results and edge details

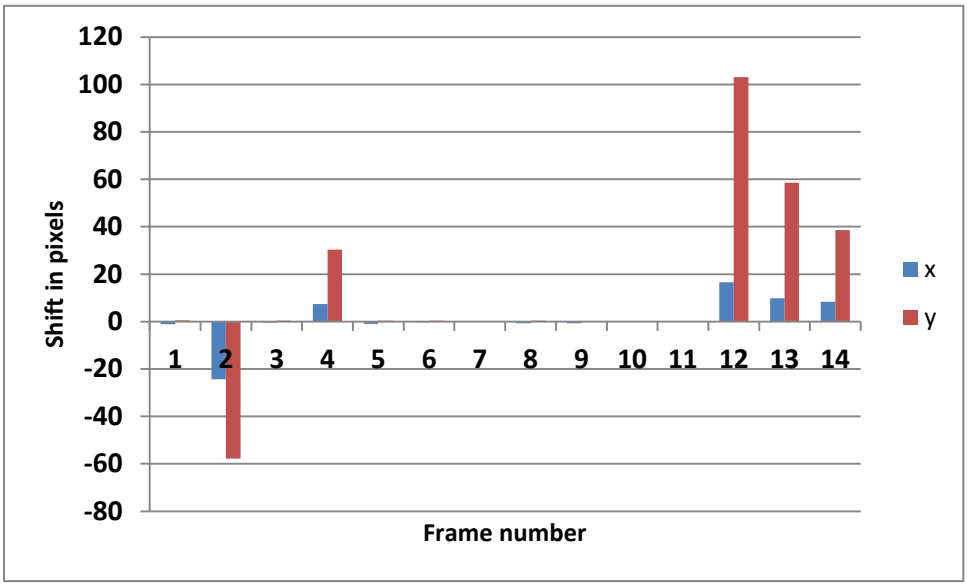

Figure 3.12 Graph showing estimated shifts without flat field (Lower the better); Frame 11 is reference; Abnormal shift as high as 100 pixels is undesirable

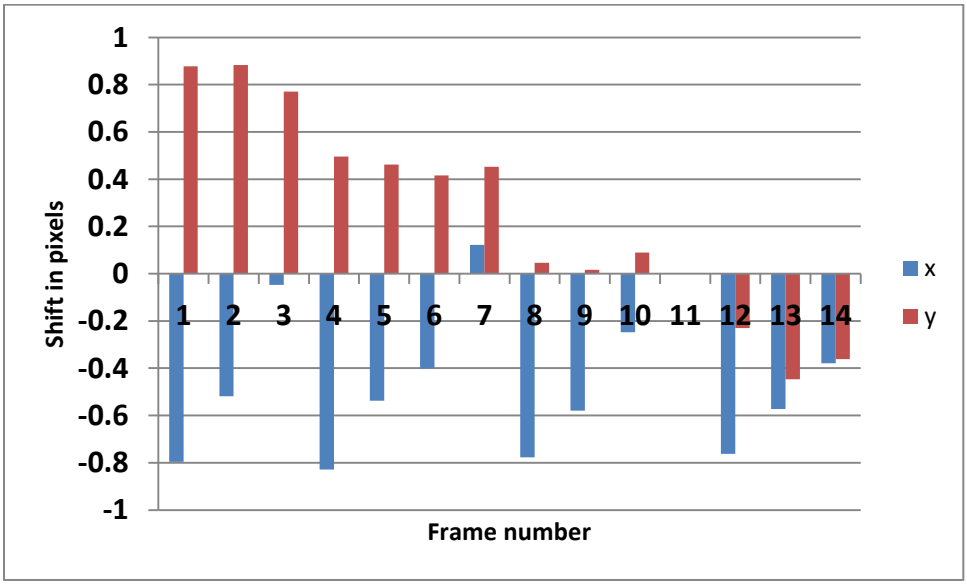

Figure 3.13 Graph showing estimated shifts with pseudo flat field (Lower the better); Frame 11 is reference

Chapter 4 Super Resolution Method

4.1 Introduction

In this chapter, the method of super resolution yielding in less amount of time is discussed with different applications. With the main application in microscopy, this method produces excellent results for doing red blood cells and white blood cells analysis.

The low resolution images are captured from the same scene with different subpixel shifts. These low resolution images contain noise, camera blur effect; camera point spread function, downsampling effect and atmospheric blur effect. For estimating the high resolution model, it necessary to assume the noise model of low resolution image. If it doesn't meet the criteria of low resolution model then the system performance is affected considerably. The fast super resolution method used in this thesis is robust and applies to any low resolution image sets as long as there is preconditioning of subpixel shift between these images.

The main objective is to produce super resolved image in least amount of time with more details which has high pixel values. The algorithm presented deals with displacement values which are, two dimension motion shifts for all the LR corrupted images with respect to the reference LR image. If we have set of n images and first image is considered as reference image, then $n-1$ horizontal and vertical shifts should have real floating values.

The motion estimation algorithm which is the optical flow algorithm is applied to green channel of the image. It is assumed that the subpixel shift is same for all the channels which are necessary because if the shift is different for different channel then the result will be a blurry image with incorrect pixel values in the high resolution image.

Scene formation

(a) High Resolution image (Lena)

(b) Geometric Transformation F_k

(c) Optical Blur H_k

(d) Sampling D_k

(e) Low resolution image with noise

Figure 4.1 Scene formation with degradation of original scene [3]

High resolution image can be written as linear operators through the following equation

$$HR = D_k H_k F_k . LR \tag{4.1}$$

4.2 Approach

4.2.1 Observation Model

Reconstructing super resolved image not only depends upon low resolution images but also on some assumptions and the model chosen. There are several super resolution models have been proposed which are for series of images, single image or a video sequence [3-5][10][23][63]. In this thesis, the model is taken for images with subpixel motion between LR images and which are taken from the same source. Consider LR images of size, $N_1 \times N_2$ .Consider HR image of size $L_1 N_1 \times L_2 N_2$

Also, let series of ideal images which is sampled equal to or more than Nyquist rate, be represented by:

$$x = [x_1, x_2 \ldots . x_N]^T \tag{4.2}$$

The downsampling parameters are L_1 for vertical direction and L_2 for horizontal direction. It is assumed that the downsampling parameter remains constant during acquisition of multiple LR images. The motion between them is random which is estimated by optical flow method mentioned in the previous chapter. These observed LR images are result of translation or rotation in the images, blur which corresponds to optical blur; motion blur and sensor point spread function, which are the limitations of economic imaging system. These images are assumed to subsample of HR image which are further corrupted by additive noise.

For simplified version the blur, decimation are assumed equal or with minute difference between the frames respectively. Our goal is to recover the HR image $\underline{X}$ from corrupted low resolution images $Y_1 \ldots Y_n$.

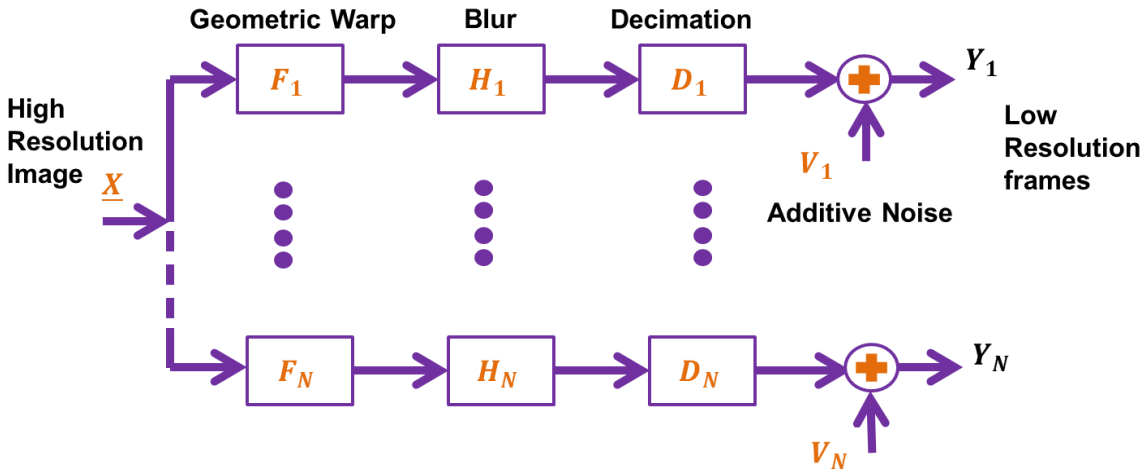

Figure 4.2 Super resolution model

$$Y_k = \{D_k H_k F_k \underline{X} + \underline{V_k} \sim N\{0, \sigma_n^2\}\}_{k=1}^{N} \tag{4.3}$$

There are several solutions proposed for this problem [3][15] but they suffer from the time complexity which our algorithm fixes with similar to better results. Some of the solutions require the blur operation in order to process these LR images.

The basic idea to obtain a super resolved image is the availability of multiple LR images. These LR images are aliased and there is movement of subpixel precision which is important because if there is integer shift then there is no new information present and the reconstruction would not be possible.

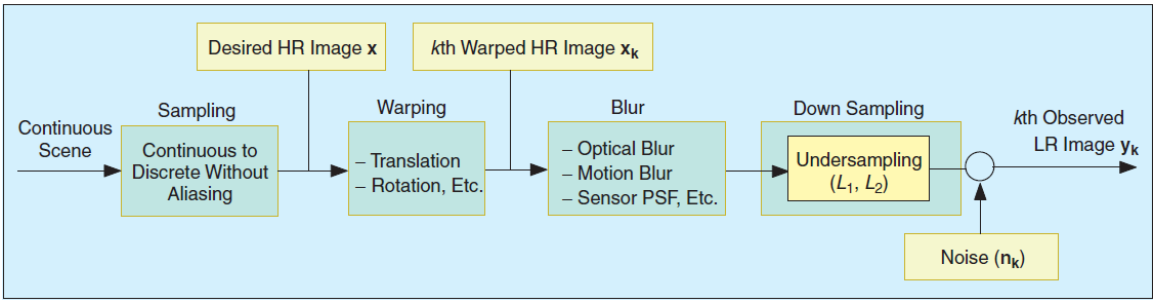

Figure 4.3 Observation Model [7]

4.2.2 Shift Fusion

For preconditioning, we have sequence of low resolution image, displacement vector for each frame $\{d_{1,2\ldots k}\}$, registered and PFFC corrected LR frames $\{r_{1,2\ldots k}\}$ and initial resolution factor set to two which is the size by the amount HR image will be reconstructed.

Motion estimation is completed through optical flow method which gives a vector of displacement values. This vector contains horizontal and vertical shifts. For each frame, if displacement exists in the form of subpixel motion, the algorithm scans through each pixel position for values in horizontal and vertical direction respectively. The displacement vector V has values defined from integer $d = 2$ to $d = r - 1$ where r is the resolution factor. Following table shows the logical displacement vector.

Table 4.1 Displacement estimated shown for frames 1-8 in x and y direction for a sample image, with I_1 as the reference frame.

Frame	x	y
I_1	0	0
I_2	2	3
I_3	3	3
I_4	3	2
I_5	3	3
I_6	2	3
I_7	3	3
I_8	2	3

Table 4.2 Displacement vector showing logical values for $x = 2$ and $y = 3$. Only displacement found in the images are accounted for computation. In this particular case, Frames I_2, I_6, I_8 are used to calculate the actual pixel value in high resolution image.

Frame number	V
I_1	False
I_2	True
I_3	False
I_4	False
I_5	False
I_6	True
I_7	False
I_8	True

Array V contains displacement values which are determined by motion estimation method. LR frames containing true values are used computation. High resolution grid gets filled by calculating the mean of all the shifts of LR frames with true values in the displacement vector. Instead of taking mean of all the LR frames, we fill pixel position in the high resolution grid with the mean of only those LR frames for which the displacement is true, which in this case would be $x = 2,4,6 \ldots . . M$ and $y = 3,5,7,9 \ldots . . N$. In Table 4.2, only $2^{nd}, 6^{th}\ and\ 8^{th}$ frames are considered and rest are discarded. Let I_m be true pixel value, which is calculated by,

$$I_m = \frac{I_2 + I_6 + I_8}{3} \tag{4.4}$$

This is considerably improved method in time and memory which still provides very good result. This is an efficient and robust approach to find the super resolution image by determining correct pixel value in current channel being computed upon. This fusion is done for red, green and blue channels which are combined to form a color RGB image. Motion estimation is crucial because it ultimately depends upon the correct shifts calculated from the optical flow method for proper formation of high resolution image. For n relevant LR frames having the same displacement value $\{I_{1,2 \ldots n}\}$, are fused together onto HR grid with increasing value of $, y = 1,2 \ldots r - 1$, where r is final

resolution factor. Following figures $4.4 - 4.8$ shows an example of working of our method.

0	0	0	0	0	0	0	0
0	133.5754	0	114.9767	0	123.0461	0	114.9512
0	0	0	0	0	0	0	0
0	114.8466	0	90.54543	0	75.97675	0	80.39474
0	0	0	0	0	0	0	0
0	106.7424	0	77.08707	0	82.71059	0	100.3523
0	0	0	0	0	0	0	0
0	78.64569	0	81.61424	0	86.47587	0	91.58139

Figure 4.4 HR image matrix showing pixel values (Image size is 8x8 pixels) and every 2^{nd} pixel corresponds to correct pixel value calculated from mean of relevant LR frames with same displacement value.

0	0	0	0	0	0	0	0
0	133.5754	0	114.9767	0	123.0461	0	114.9512
0	112.4535	0	122.7317	0	78.75675	0	71.20492
0	114.8466	0	90.54543	0	75.97675	0	80.39474
0	72.84331	0	89.99882	0	84.36152	0	76.05898
0	106.7424	0	77.08707	0	82.71059	0	100.3523
0	89.99882	0	108.1296	0	109.1509	0	120.6093
0	78.64569	0	81.61424	0	86.47587	0	91.58139

Figure 4.5 Every 2^{nd} pixel value in y-direction after calculations

0	0	0	0	0	0	0	0
0	133.5754	68.6665	114.9767	58.97914	123.0461	61.9503	114.9512
0	112.4535	0	122.7317	0	78.75675	0	71.20492
0	114.8466	80.38284	90.54543	55.27473	75.97675	54.10828	80.39474
0	72.84331	0	89.99882	0	84.36152	0	76.05898
0	106.7424	71.06532	77.08707	80.60895	82.71059	75.84409	100.3523
0	89.99882	0	108.1296	0	109.1509	0	120.6093
0	78.64569	68.37851	81.61424	101.1639	86.47587	99.05487	91.58139

Figure 4.6 Every 3^{rd} pixel value in x-direction after calculations

0	0	0	0	0	0	0	0
0	133.5754	68.6665	114.9767	58.97914	123.0461	61.9503	114.9512
0	112.4535	120.5076	122.7317	94.86072	78.75675	76.9139	71.20492
0	114.8466	80.38284	90.54543	55.27473	75.97675	54.10828	80.39474
0	72.84331	133.6093	89.99882	95.02873	84.36152	79.4232	76.05898
0	106.7424	71.06532	77.08707	80.60895	82.71059	75.84409	100.3523
0	89.99882	122.6585	108.1296	107.8071	109.1509	92.80192	120.6093
0	78.64569	68.37851	81.61424	101.1639	86.47587	99.05487	91.58139

Figure 4.7 Every 3^{rd} pixel value in y-direction after calculations. First row and columns are undetermined values.

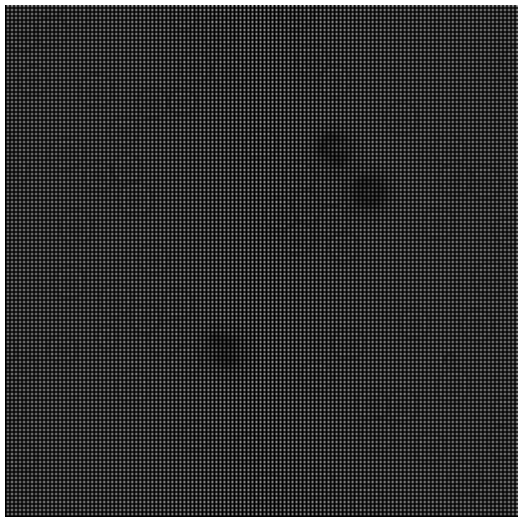

(a) HR frame, first round evaluation (256x256 pixels)

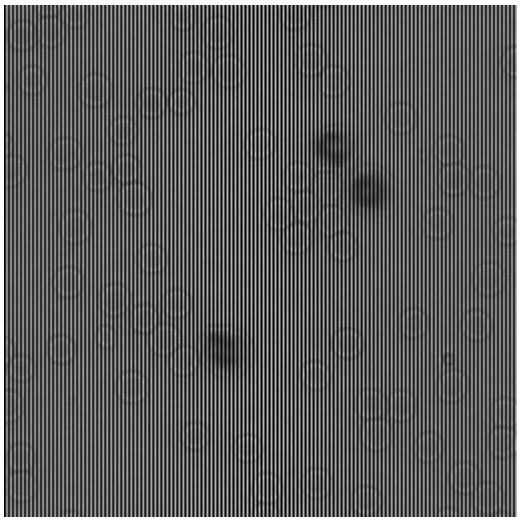

(b) HR frame, second round evaluation (256x256 pixels)

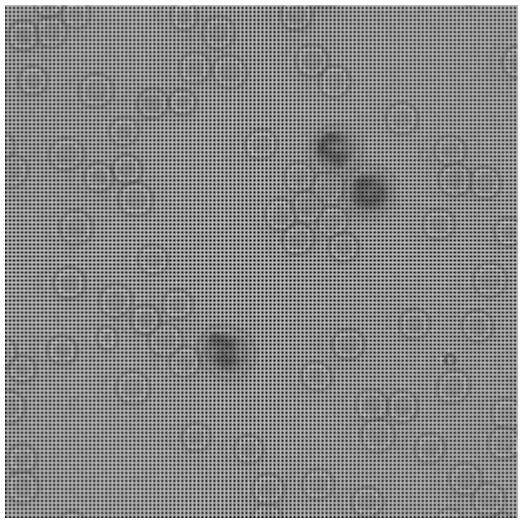

(c) HR frame, third round evaluation (256x256 pixels)

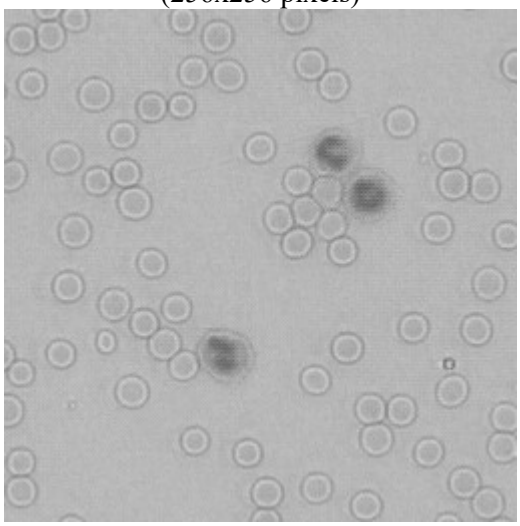

(d) Estimation of HR frame, final round evaluation (256x256 pixels)

Figure 4.8 Estimation of HR frame

Table 4.3 Area, and Intensity values for the images generated by filling of pixel values

Image	Area (pixels)	Minimum intensity	Maximum intensity
4.8 (a)	65536	45.224	0
4.8 (b)	65536	89.910	0
4.8 (c)	65536	135.138	0
4.8 (d)	65536	180.193	95

After completing the previous step, we arrive at the first estimation of super resolved image Z through these low sequences frame. For undetermined shifts where the

pixel values are not filled, have a current value equal to zero. In order to find these values, a separate empty HR grid Z_{med} is created. Kernel size of median filter is initial resolution factor which is computed for image Z as shown in the following equation.

$$Z_{med} = medfilt2(Z[\, L_1N_1 \times L_2N_2]) \tag{4.5}$$

The undetermined pixel values calculated in Z_{med} are inserted into image Z. All the values in high resolution grid are determined which gives the super resolved image. After obtaining all the pixel values, the image is resampled with Lanczos or bicubic filter of size s from (4.5) which doesn't lose much detail in order to further analyze the image, for example, doing segmentation and classification of blood cell types. Here, the time process is greatly reduced compared to other methods [3-4][56][57] as our method takes advantange initial reconstruction which is twice the size of LR.

$$s = \sqrt{N_1 \times N_2}\Big/_2 \tag{4.6}$$

The noise reduction is done through a median filter which is excellent in preserving edges. We found that, the results using regularization compared with our result are comparatively same with huge amount of time calculation, our method saves time and provides reconstructed image which on which segmentation can be analyzed. This is found useful in determining the edges and nucleus of blood cells in the images which is crucial for classification of white blood cells. The kernel size ranges from 2 to 5. It is important to note that if the size of kernel is very high then the resultant image will be blurred.

4.3 Conclusion

This chapter, we described an efficient method to process low resolution images. We discussed the observational model used and solved equation built upon assumptions of noise and blur factor in the low resolution frames. Looping over the entire high resolution grid and generating the super resolution image was also shown with an example of how pixel value is calculated from the low resolution frames which accounts for correct intensity value in the high resolution grid.

Chapter 5 Results and Analysis

In this chapter, we show the results obtained by implementing our super resolution method on images captured in various environments. Firstly, synthetic images from popular datasets processed to reconstruct high resolution image. Real world images taken from the lens-less devices are also processed upon and results are shown. Time and detail comparison with different super resolution methods is made. Qualitative analysis of images is done through visual inspection comparing to ground truth image if it is available or comparing with low resolution image and quantitative analysis is employed through visual perception, SSIM index and intensity profile plot.

Details of images are seen through image edge detection through Sobel method comparing with image edges of low resolution image and other super resolution methods.

5.1 Qualitative Analysis of Images

A set of 6 grayscale images and 3 colour images are taken from dataset [48][58]. Our algorithm is implemented on these images and results are shown. These real world images are captured from a camera and are chosen from wide variety of environment to robustness of our super resolution method. There is significant improvement of resolution noticed with more than resolution factor of 2.

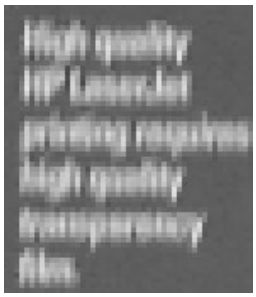

a.) Text sequence

b.) Car sequence

c.) Alpaca sequence

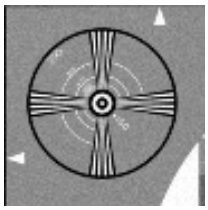

d.) EIA sequence

e.) Grayscale face sequence

f.) Color face

g.) Bookcase

h.) Adyoron

Figure 5.1 Image datasets for super resolution reconstruction

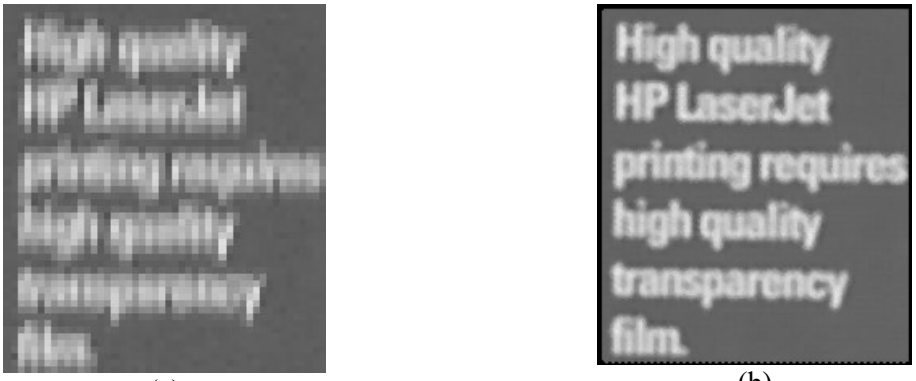

(a) (b)

Figure 5.2 Low resolution frame $(1/30)$ of Text image compared to our reconstructed result (b) with resolution improvement by factor of 4. The text clearly reads "*High quality HP LaserJet printing requires high quality transparency film*". There is huge amount of noise reduction and improvement in resolution. Initial size of image is 49x57 pixels and reconstructed image size is 195×223

(a) (b)

Figure 5.3 Low resolution frame of moving car sequence $(1/10)$. Only 10 frames out of 64 were processed in the region of license plate to reconstruct super resolved image. Improvement of resolution is visible where an unreadable license plate reads "*3PLK273*", as well as the car model reads "*SUBARU*" proving improvement of resolution. This is one of the powerful applications of super resolution shown by our fast working algorithm where it is useful. This image was computed in 0.51 seconds. The LR images are of size 72×121 pixels and reconstructed image is of size 216×363.

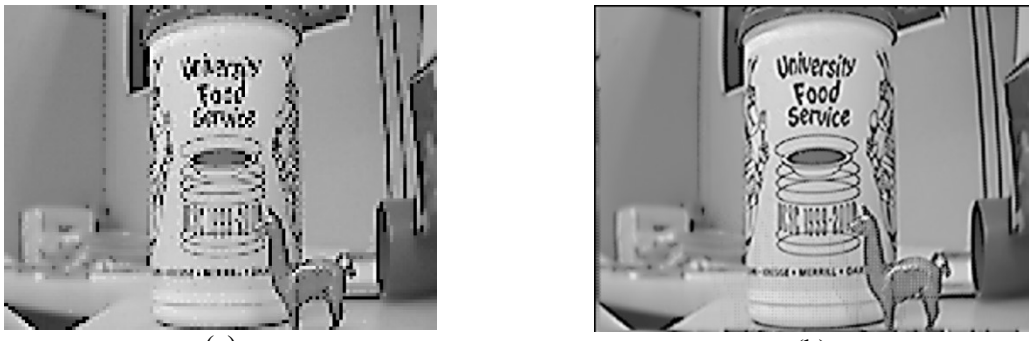

(a) (b)

Figure 5.4 Low resolution Alpaca sequence shown in (a) which is (1/55) frame and reconstructed result shown in (b). The LR sequence is of size 128×96 pixels and super resolved image is of size 514×386 pixels. The text shown can be read clearly: *"University Food Service*". From pixelated image to fine defined prints seen in text, numbers and shape of alpaca, our method works in this scenario as well.

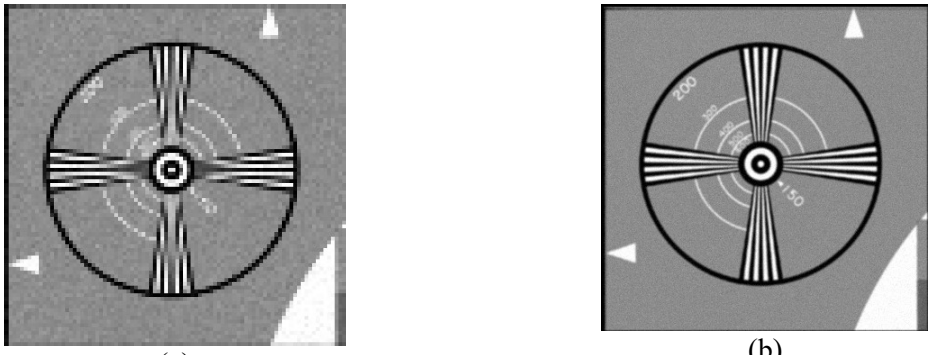

(a) (b)

Figure 5.5 (a) showing EIA low resolution frame (1/16) and reconstructed image is shown in (b). The improvement in formation of circle, triangle lines and readable text is crystal clear. Resolution improvement is a factor of 4. The input image size is 90×90 and output image size is 363×363. The image is shrunken to fit the page.

(a) (b)

Figure 5.6 Grayscale face low resolution frame (1/60) shown in (a) and reconstructed result is shown in (b). This is also one of the popular applications by super resolution for security. Glasses are clearly visible and improvement in resolution is seen in structure of face. The input image is of size 34×38 pixels and resultant image is of size 138×154 pixels.

Following images are results for color images. Motion between the low resolution frames is estimated only through one channel which is green channel instead of three color channels which saves considerable amount of time and gives better results as shifts are assumed same for all channels.

(a) (b)

Figure 5.7 Low resolution colour frame of books (1/30) shown in (a) and reconstruction result shown in (b). The gain in resolution is visible through readable titles of the textbook. Some of unreadable texts such as Kalman Filtering, Robust Statistics and the book on the right "Digital Signal Processing" with subtitle "Computer Based Approach". This result shows that our algorithm works great with colour images as well. The input image is of size 121×91 pixels and output image is of size 484×364 pixels with resolution improvement of factor of 4.

(a) (b)

Figure 5.8 Low resolution Adyoron image $(1/40)$ shown in (a) of size 138×115 pixels and super resolved image obtained by our method shown in (b). The resultant image is of size 414×345 pixels.

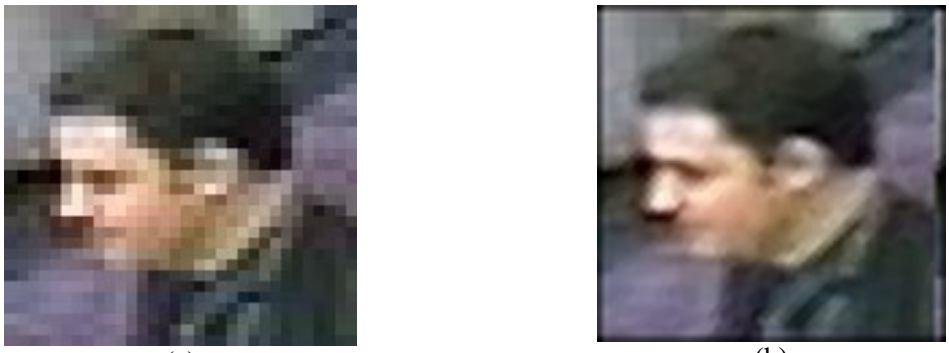

(a) (b)

Figure 5.9 An application of color CCTV camera capturing frame (1/40) shown in (a) and result shown in (b). The face is clearly visible with distinguishable facial features. The input image is of size 32×31 pixels and resultant image is of size 130×126 pixels.

5.2 Assessment using Synthetic Images

In this section the quantitative analysis of images is done through plotting Intensity Profile and calculating Structural Similarity Index (SSIM) for each image. A set of 12 images is chosen [48][49] as shown in Figure 5.11 which are downsampled to generate 10 low resolution frames with random motion in each of them. We apply our method to reconstruct the image and compare SSIM index value with the original image. Higher SSIM indicates good result which is displayed in Table 5.1. Improvement of SSIM is more than 1.5 times is seen than the low resolution image. Compared with [3], our method out performed index performance as seen in Table 5.1. The comparison data is shown graphically in Figure 5.14.

Intensity profile is set of intensity values for a particular region in an image. It is useful entity to see the sharpness and peaks of the region under consideration. Image having high resolution have set of different peaks without discrete quantities. Low resolution images suffer from discrete intensities and random peaks in the profile. This method is useful to distinguish between a low resolution image and high resolution image [58-60].

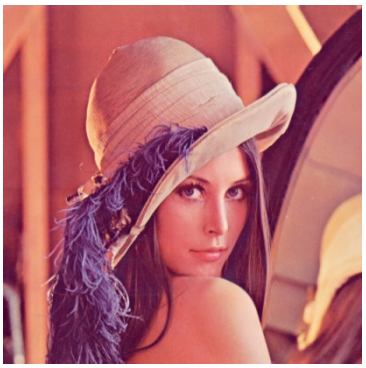

(a) Lena ($512 \times 512\ pixels$)

(b) Mandrill ($512 \times 512\ pixels$)

(c) Peppers ($512 \times 512\ pixels$)

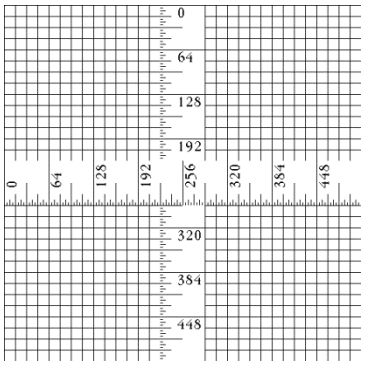

(d) Ruler ($512 \times 512\ pixels$)

(c) Aerial ($512 \times 512\ pixels$)

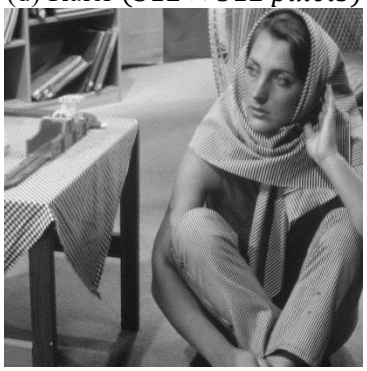

(d) Barbara ($512 \times 512\ pixels$)

(e) Boat ($512 \times 512\ pixels$)

(f) Cat ($490 \times 733 pixels$)

(g) Watch ($1024 \times 768\ pixels$)

Figure 5.10 Images chosen for generation of low resolution frames. 16 frames were generated with unknown motion parameters and processed through or super resolution algorithm.

Figure 5.11 Low resolution frames generated with random shifts. Above are the frames 1,3,6,8 respectively out of 16 frames for Lena image. The original image was downsampled by a factor of 4 and random shifts in horizontal and vertical direction were introduced. Our algorithm works and produce excellent result in reproducing fast and improved resultant image. The original image is 512×512 pixels which was downsampled to 128×128 pixels.

(a) Low resolution

(b) Original Image

(c) Our result

Figure 5.12 LR image is magnified (original size is 128x128 pixels). Reconstructed size if 512x512 pixels. SSIM for the result is 0.6737

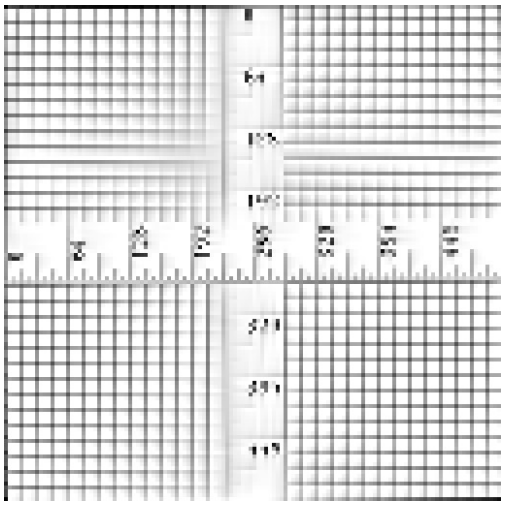

(a) Low resolution

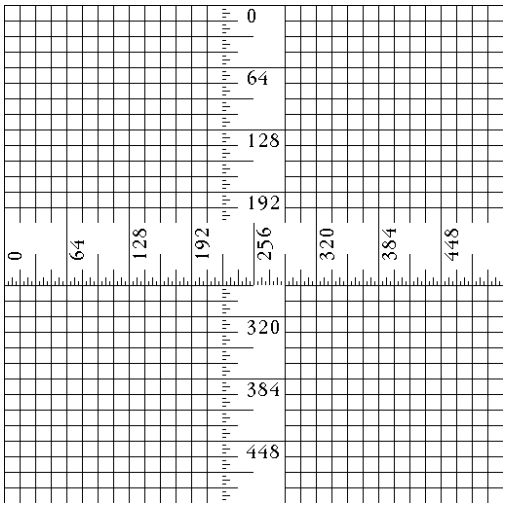

(b) Original Image

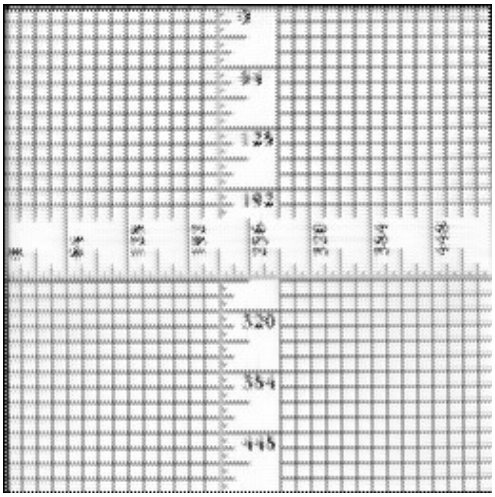

(c) Result using 10 frames

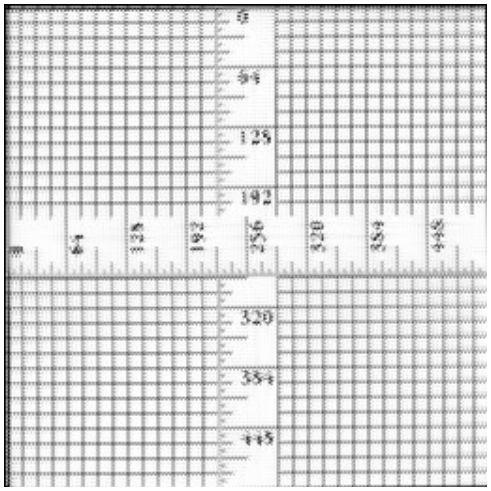

(d) Result using 20 frames

Figure 5.13 An example of number of availability of LR frames affecting the result. More number of frames gives better results as there is more information captured until a convergence is obtained. Here result through 20 frames (d) is better than 10 frames (c) as the numbers can be clearly seen in Figure (d) compared to result with Figure (c)

Table 5.1 SSIM Index values; Perfect SSIM is 1.

Image	LR image magnified	Our method	Farsiu et al. [3]
Lena	0.6083	0.7600	0.7573
Mandrill	0.2700	0.4452	0.4373
Peppers	0.5902	0.6737	0.6654
Ruler (20 frames)	0.1948	0.3001	0.2928
Aerial	0.3675	0.5600	0.5545
Barbara	0.4976	0.6222	0.6200
Boat	0.4690	0.6678	0.6614
Cat	0.4043	0.5865	0.5276
Watch	0.5623	0.7299	0.6969

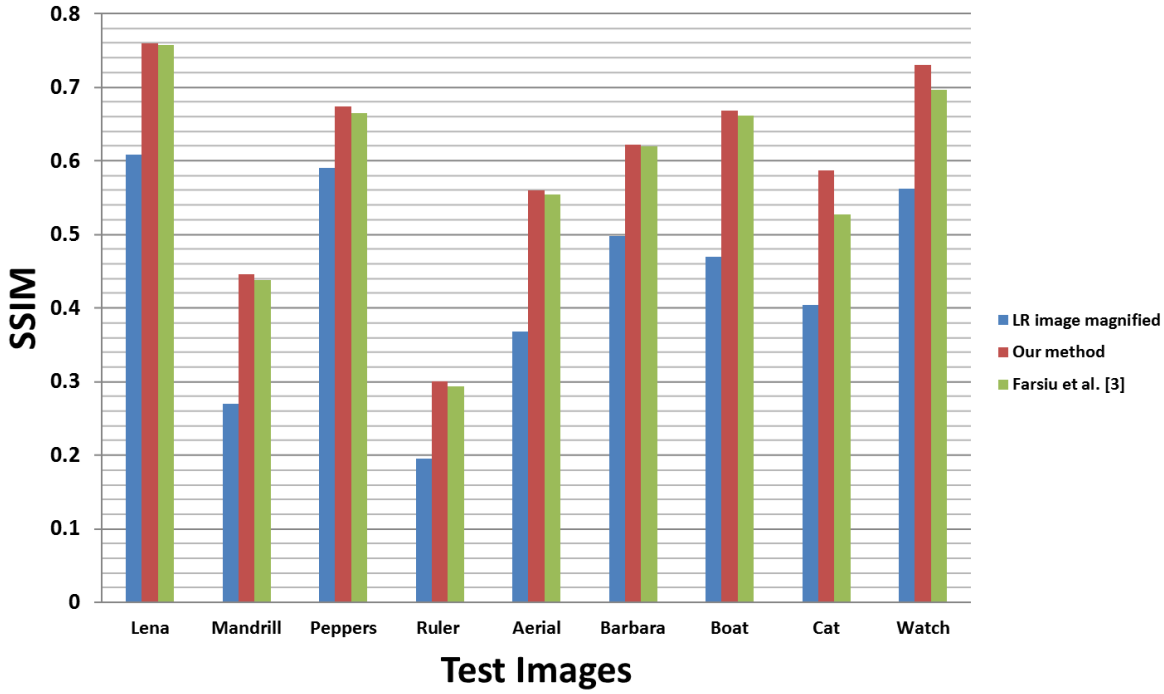

Figure 5.14 SSIM comparison chart

5.3 Analysis of Experimental Data

Collection of 18 patients was processed through our algorithm each containing 14 colour microscopic frames. Each low resolution image size is 3280×2464 pixels and final

result generated is of size 13122×9858 pixels showing improvement of resolution factor of 4. Here we show the time taken to compute our PFFC program, motion estimation and registration method and fusion method. Combining all these gives us the package of overall super resolution program.

The average time taken for each patient set was 36.24 seconds. Analysis of cellular structures is done through intensity profiling showing the intensity values for selected components of the image. We also introduce edge detection technique using Sobel method to demonstrate the improvement of resolution by showing sharp edges and visibility of nucleus inside the cells.

5.3.1 Analysis of cellular structures

Here, we show the improvement in resolution in red blood cells, white blood cells, platelets, reticulocytes and reduction in background noise. Intensity profile is generated for each of them and compared with the low resolution image. These can be further analyzed for counting, segmentation and volume purposes which is part of future study.

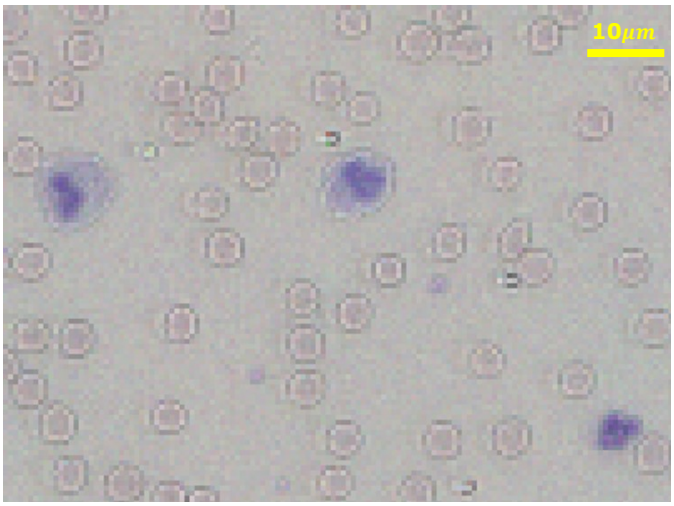

(a) LR image patch, magnified by factor of 4

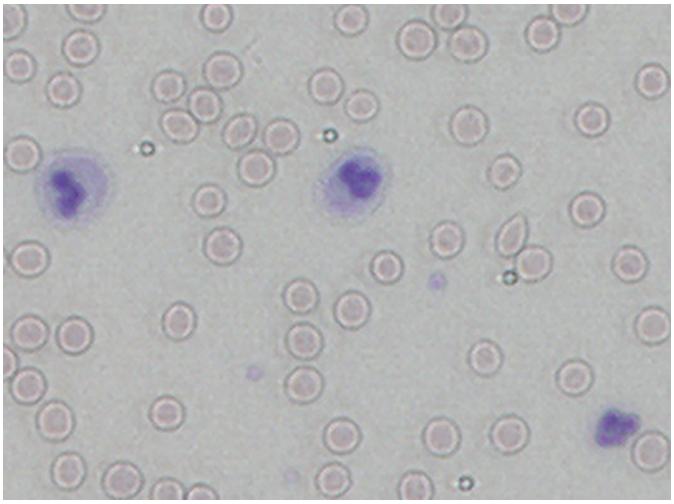

(b)

Figure 5.15 Top: Block size of 187 × 136 pixels of Frame (1/14); Image is zoomed by factor of 4. Bottom: Our result, the size of the image is 747 × 553 pixels. 1 pixel = 1.1 µm

Red Blood Cells: Following figures shows the analysis of one red blood cell in the captured image and reconstructed result.

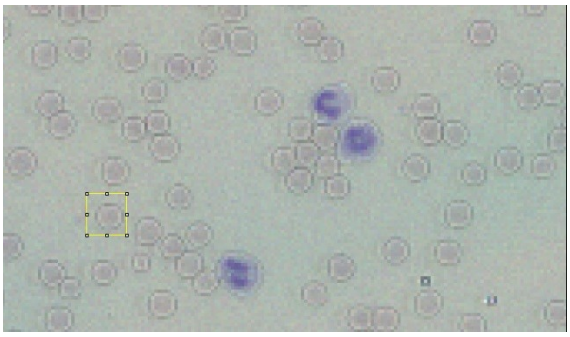

(a) LR frame

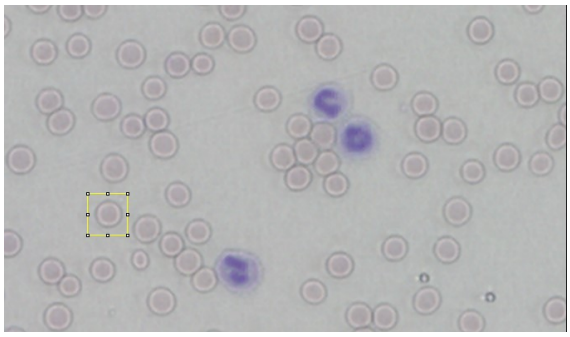

(b) SR result

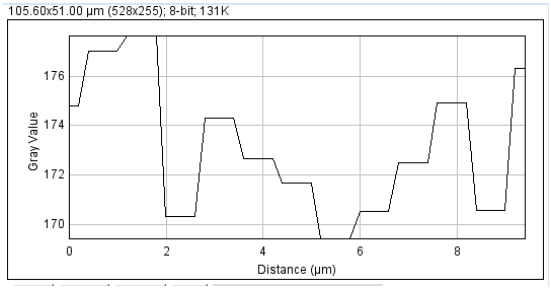

(c) Intensity profile for LR frame

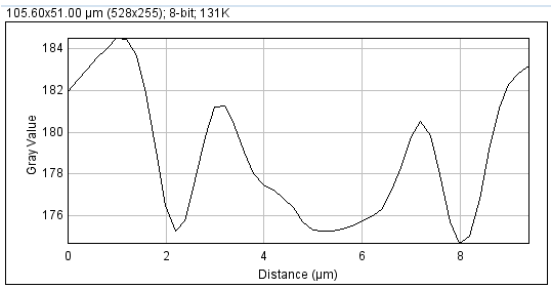

(d) Intensity profile for LR frame

Figure 5.16 Plot comparison between zoomed LR image and Super resolution result for a red blood cell

White Blood Cells:

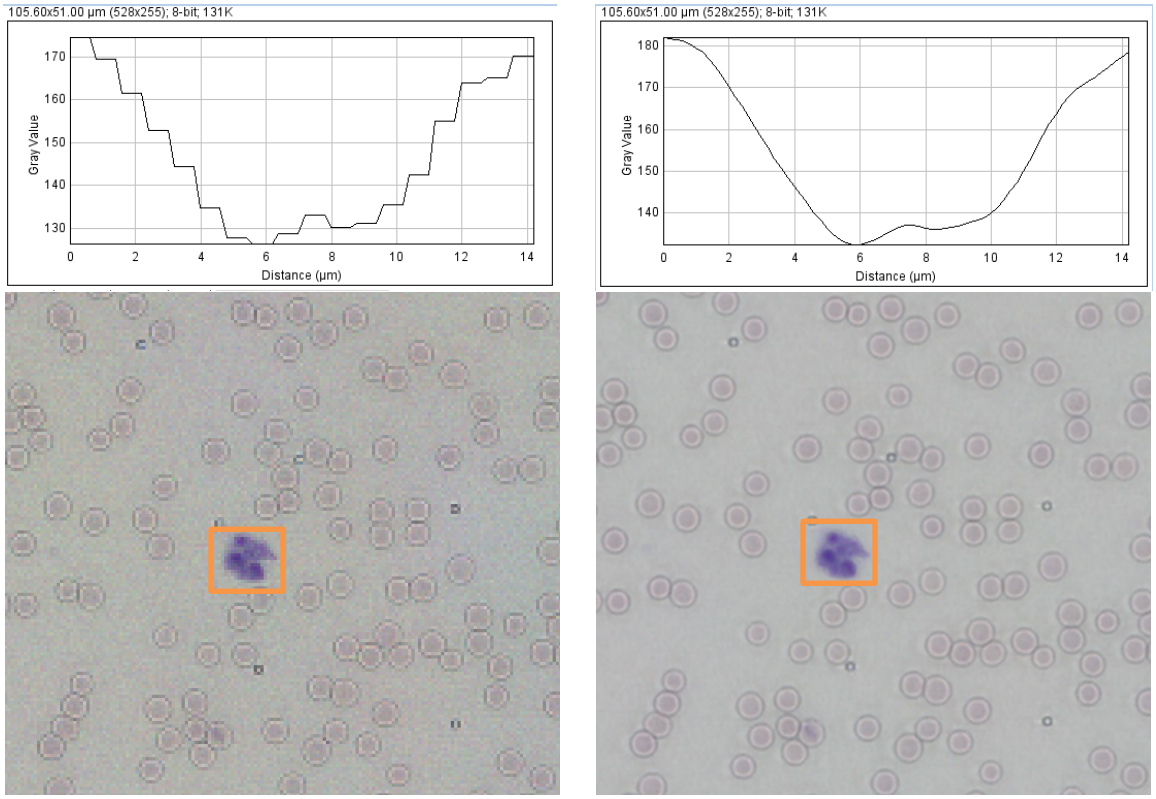

Figure 5.17 Plot comparison between zoomed LR image and Super resolution result for a white blood cell

Reticulocytes:

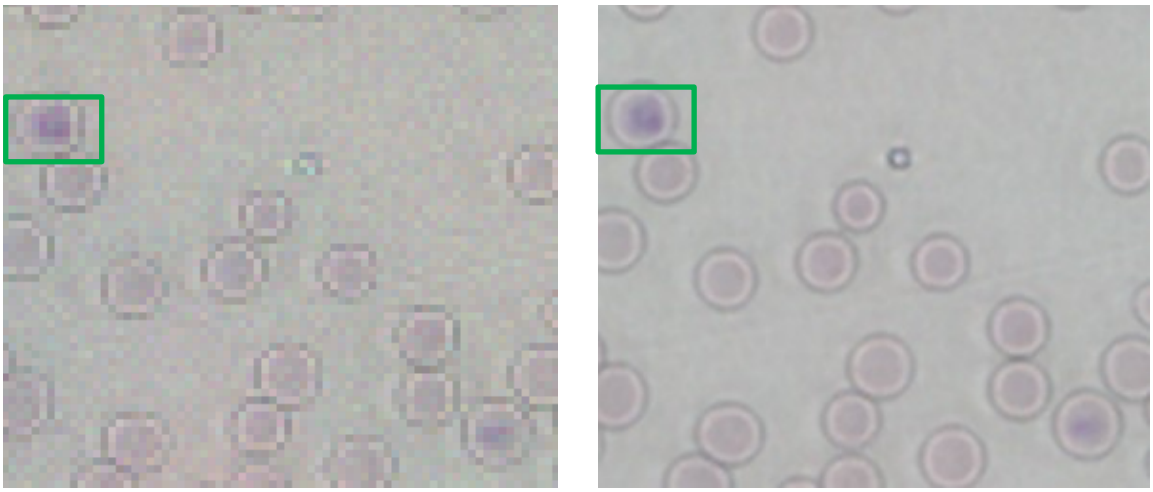

(a) LR frame (b) SR result

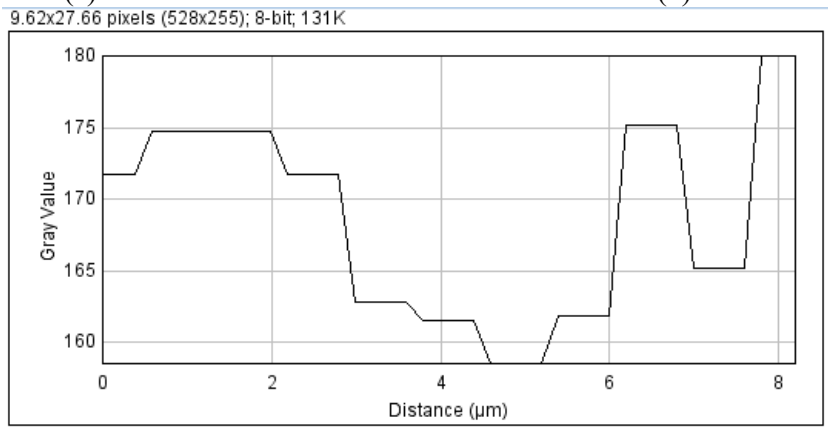

(c) Intensity profile for LR frame

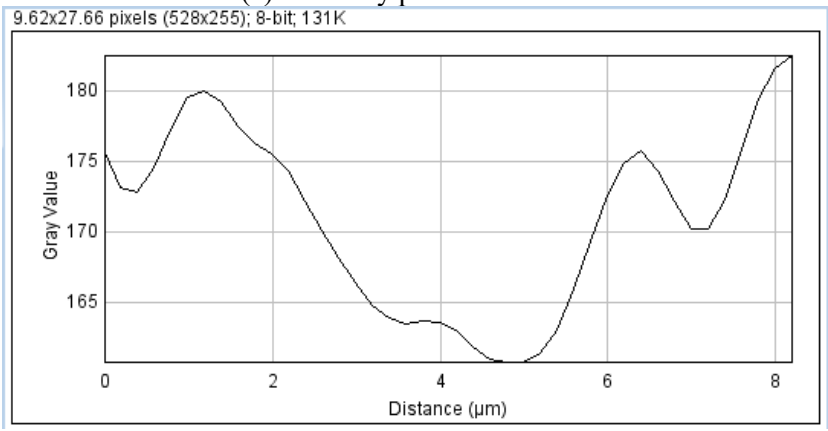

(d) Intensity profile for SR result

Figure 5.18 Plot comparison between zoomed LR image and Super resolution result for a reticulocyte.

Platelets:

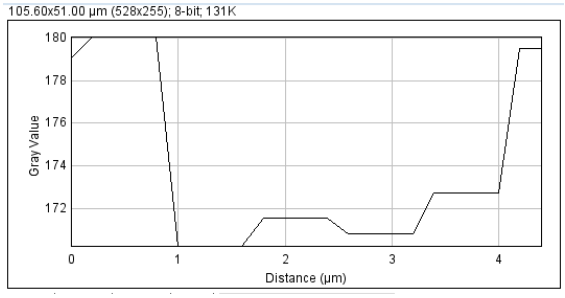

(a) LR frame

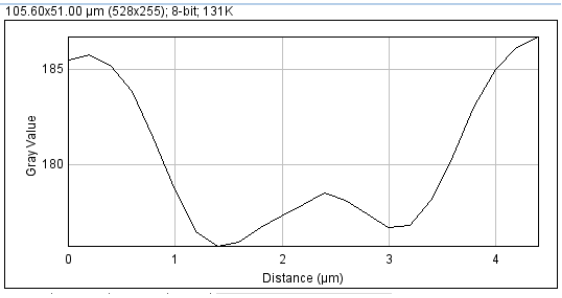

(b) SR result

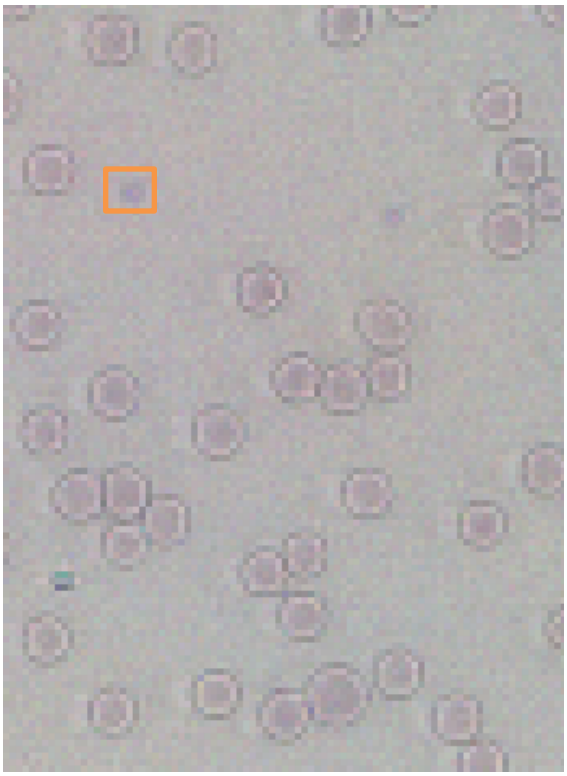

(c) Intensity profile for LR frame

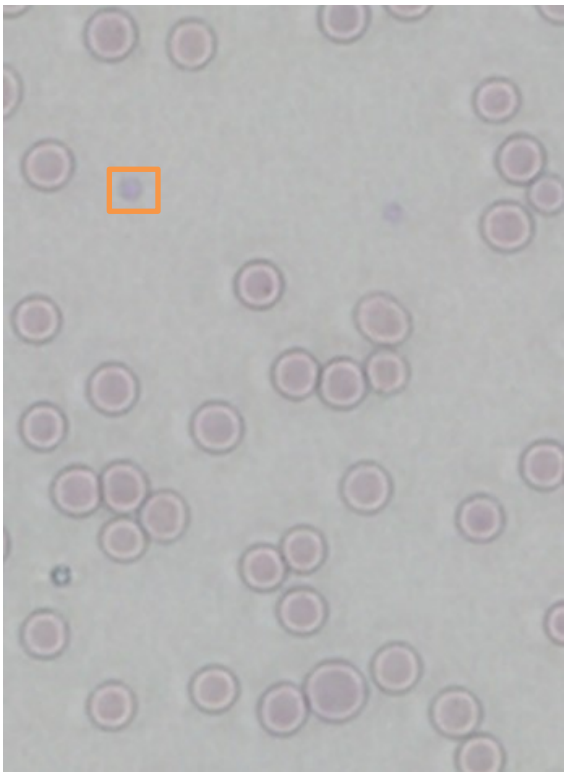

(d) Intensity profile for SR result

Figure 5.19 Plot comparison between zoomed LR image and Super resolution result for a platelet

Edge details:

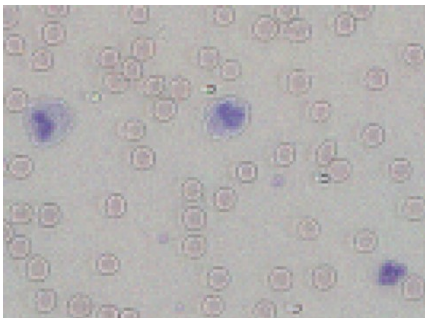

(a) Low resolution image

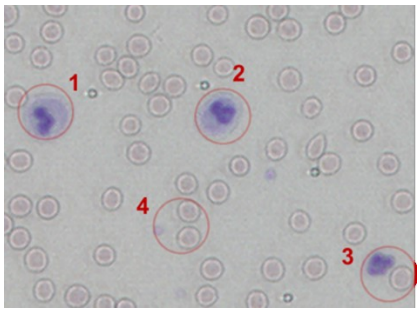

(b) Reconstruction result

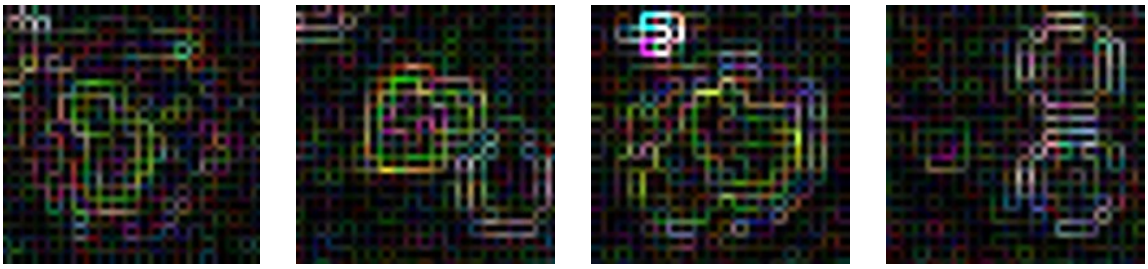

(c) Poor edge details

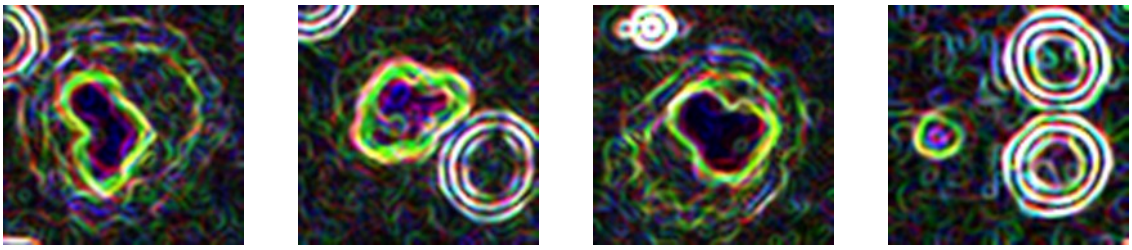

(d) Fine edge details

Figure 5.20 Sharper edges are seen for white blood cells compared to LR image acquired by the device.

5.3.2 Time complexity for Pseudo Flat Field Correction

The following figure shows time taken to compute full scale flat field correction for the whole set of experimental data. In this case, there is a set of 14 images for each patient. The size of input image is 3280×2464 pixels and it took 3.62 seconds to compute the whole dataset. This is preprocessing step before motion estimation method.

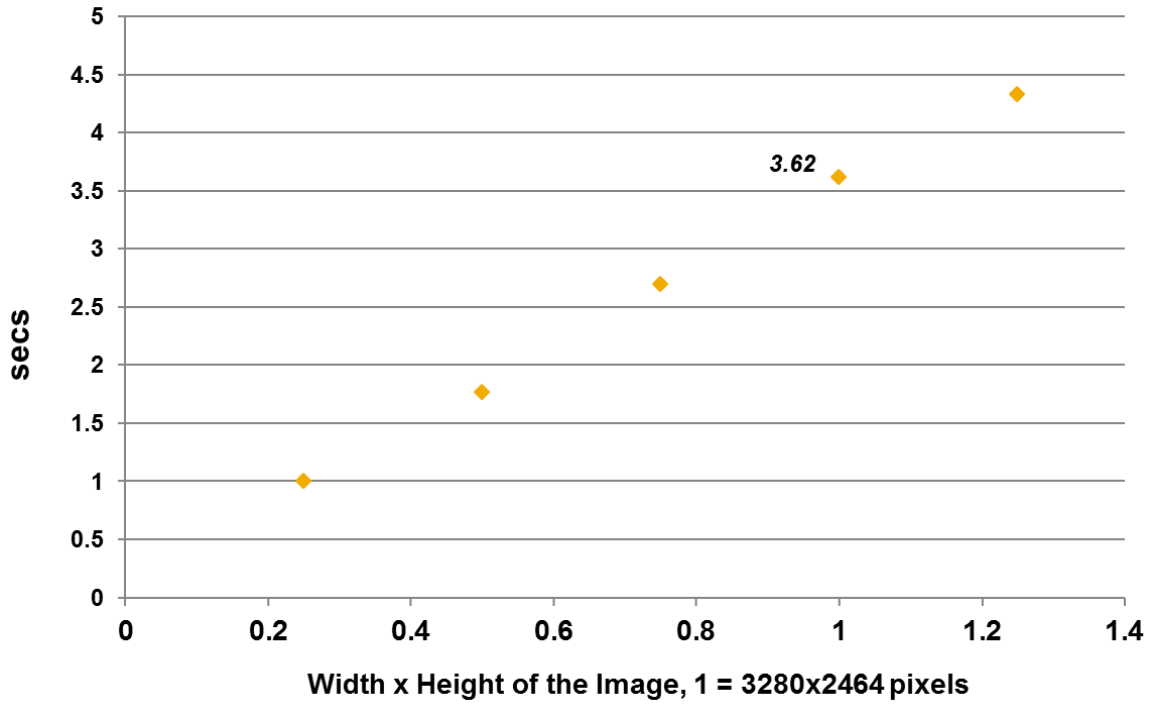

Figure 5.21 Time vs pixels for PFFC to process 14 images. Default image size is 3280 x 2464 pixels for which PFFC time is **3.62** seconds

5.3.3 Time Complexity for Super resolution method

To process the whole data set and reconstruct super resolved image, it took 36.24 seconds to do PFFC, motion estimation, registration and fusion altogether. This is incredibly fast algorithm which was processed in i5 processor with 8GB RAM. Our algorithm not only is robust but also computationally efficient. Here, x-axis ranges from $0.25s$ to s, where s is the size of reconstructed result ($13120 \times 9856\ pixels$). Time was computed for $0.25s, 0.5s, 0.75s\ and\ s$ size of the result.

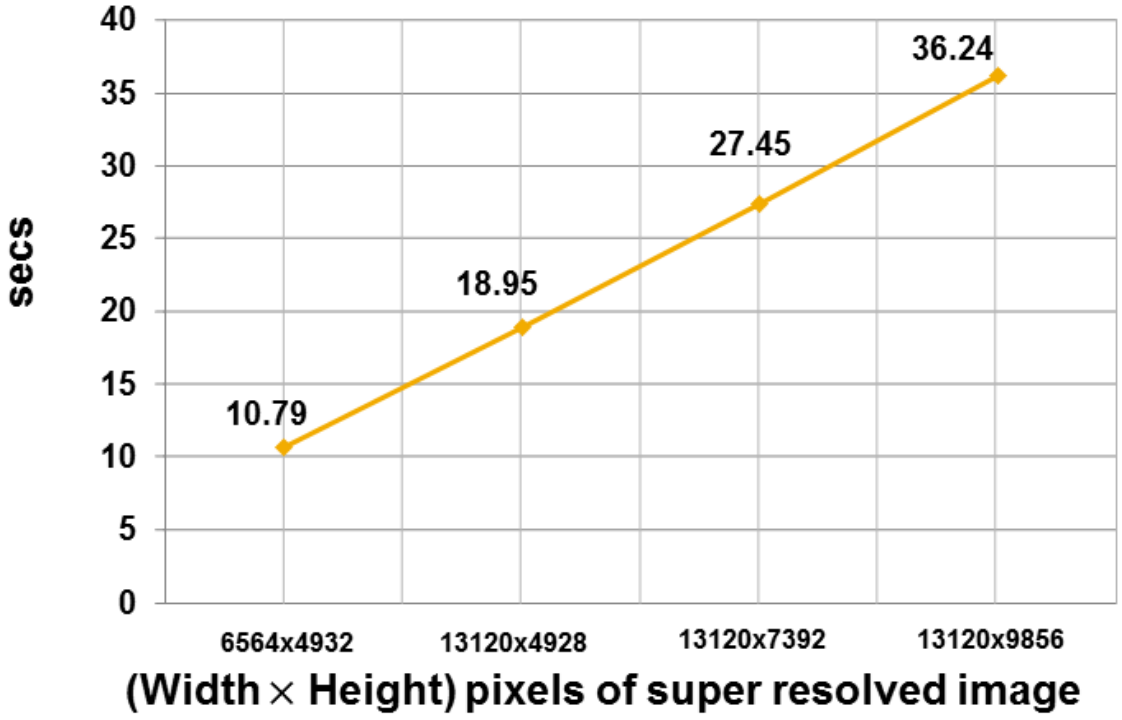

Figure 5.22 Graph showing time taken to compute super resolution method vs Total number of pixels in the reconstructed image.

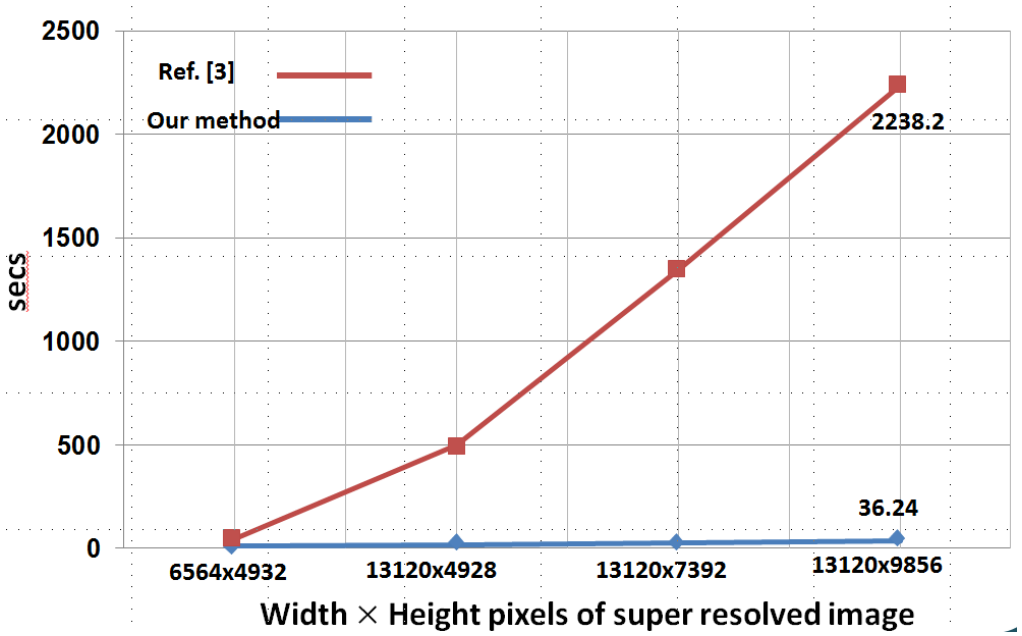

Figure 5.23 Graph showing comparison between well known super resolution method vs Our algorithm

5.4 Quantifying Resolution

For finding out true resolution improvement, we carried out tests to quantify the improvement in resolution through our reconstruction method. Resolution is measured in cycles/mm or line pairs/mm (lp/mm). At a certain point, the imaging system is limited and unable to distuinguish between the black and white line pairs. Our method breaks this limit and is able to improve and exceed the limits of the resolution. Resolution improvement of three fold was achieved.

5.5.1 Reconstruction through Simulation

Image was taken from [62] with highest resolvibility power of 3.6 lp/mm. Gaussian noise with mean zero and standard deviation of 30 was added. Downsampling by factor of 4 with a blur with random translational subpixel shifts were introduced which gave rise to 30 low resolution frames of which one of the frames is shown in figure 5.24 (a). The highest lp/mm which could be resolved in this image is below 0.79 lp/mm which can be seen from the line profile in figure 5.23 (b). At 0.89 lp/mm the lines are indistuinguishable.

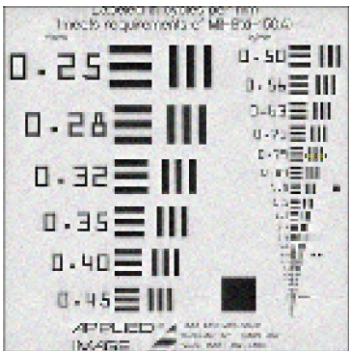

(a) LR frame

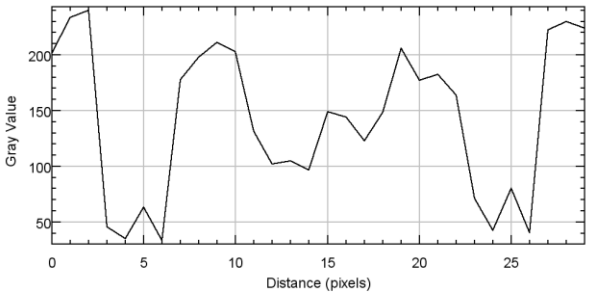

(b) Line Profile for LR frame across 0.79

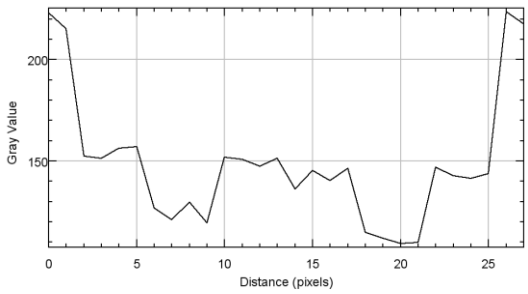

(c) Line Profile for LR frame across 0.89

Figure 5.24 Resolution limit for LR image

Reconstruction through our method is shown in Figure 5.25 with line pairs across 1.6 lp/mm and 1.8 lp/mm. Highest resolution is obtained above 1.8lp/mm and below 2.0lp/mm. Through this analysis we see that the improvement in resolution is more than 2.5 times compared to the low resolution frames which prove working of our method. For visual representation of how resolution is decreasing with increase in lp/mm, a vertical line profile has been plotted in Figure 6 for both low resolution and super resolved image respectively.

After a certain point which is disability to resolve two lines in the image is seen in the line profile which becomes constant showing same pixel value in the neighbouring area of consideration.

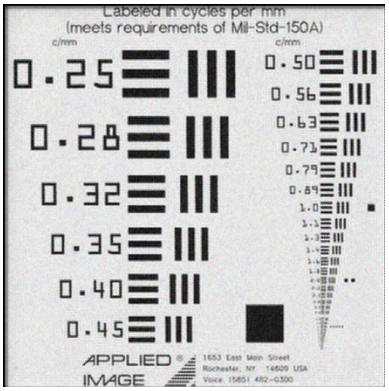

(a) Reconstruction result

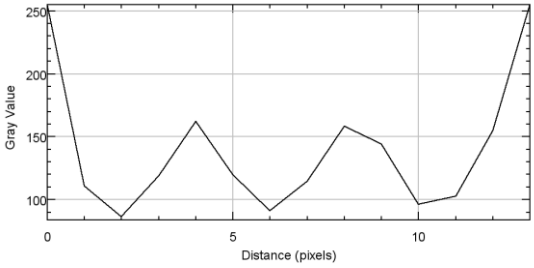

(b) Line Profile for line pairs across 1.8

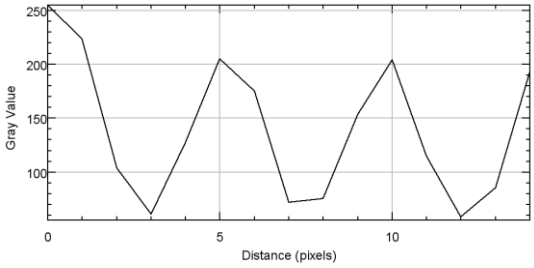

(c) Line Profile line pairs across 1.6

Figure 5.25 Resolution limit for reconstructed result

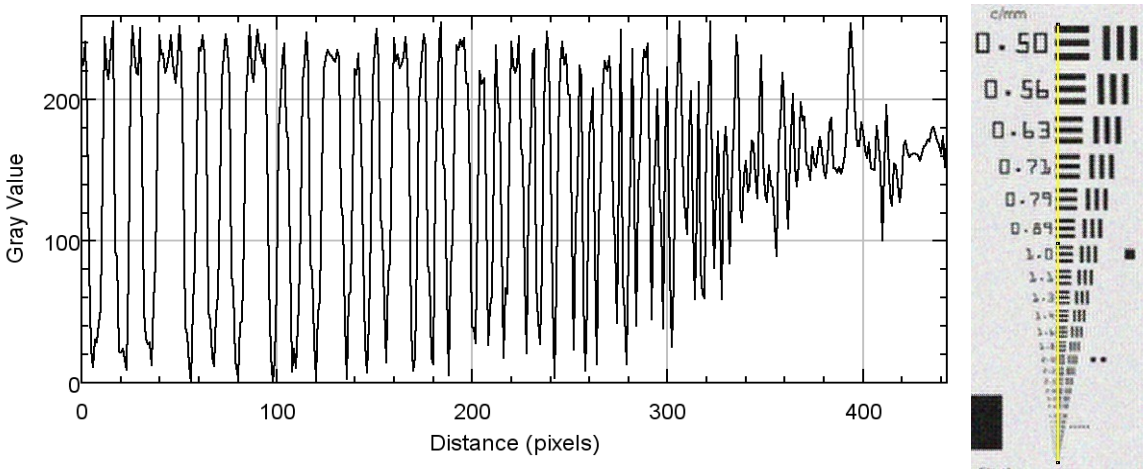

a. Vertical Line Profile for Super resolution reconstruction

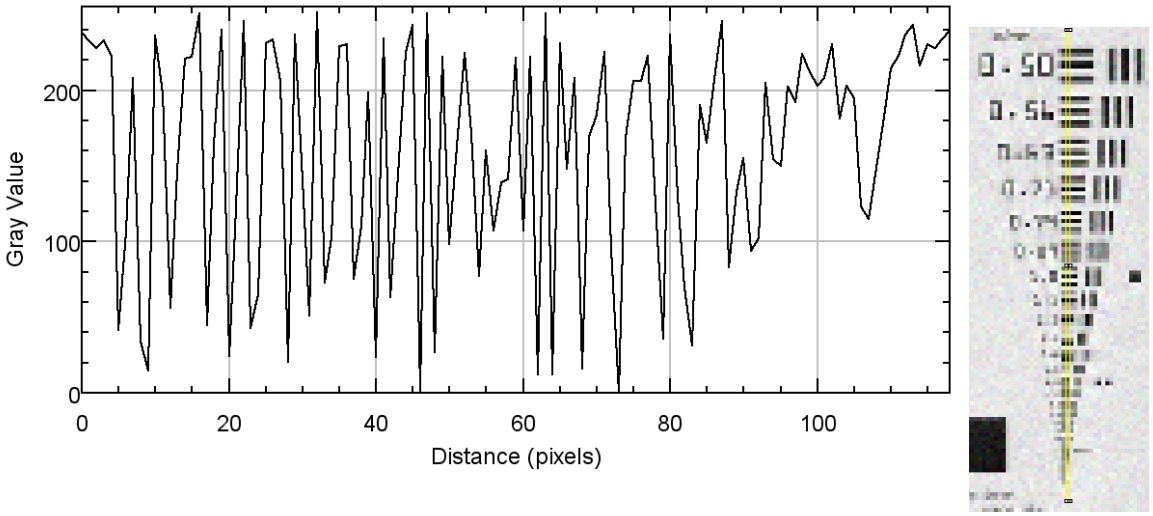

b. Vertical Line Profile for Low resolution image

Figure 5.26 True resolution improvement after reconstruction

5.5.2 Reconstruction through a mobile phone camera

To test robustness of the algorithm, an iPhone camera was used to take multiple frames of same scene with handheld position. As the movement of hands is not steady while taking photos, even a small amount of movement generates subpixel shift. The image was taken of resolution chart QA-71-P-RM by Applied Image Inc. which is a standard IEEE video resolution chart for testing the resolution of cameras [61]. It contains TVL (Television

Lines) as measure of resolution. Highest resolution is 1000 TVL/6inch which is 3.21 line pairs / mm. The following figure 5.27 shows the full scale image taken from an IPhone camera. A burst of 40 images were captured from the same scene. We found that our method increased the resolution from 2x100 TVL to 5x100 TVL. This result enables one to obtain a better understanding of the measurements and proof-of-performance of proposed method.

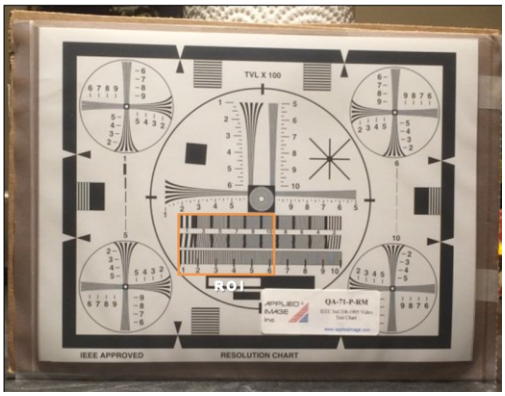

a. Full scale image of resolution chart

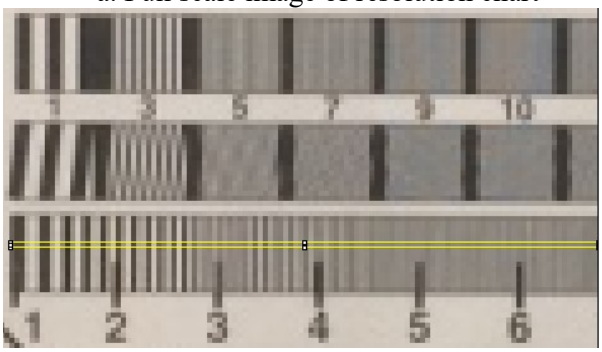

b. Zoomed (4x) region of interest

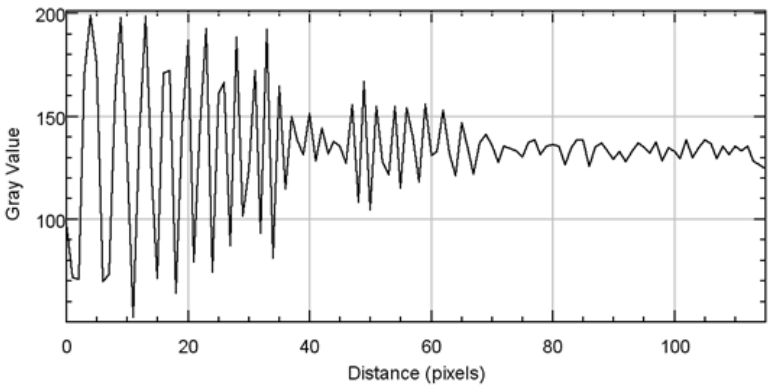

c. Line profile for zoomed region of interest

Figure 5.27 Captured image a mobile camera and it's intensity profile

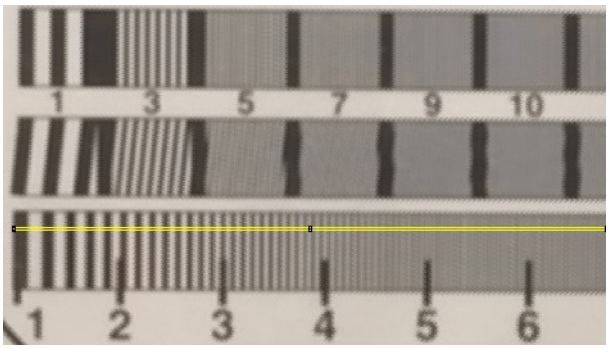

a. Super resolution image obtained by our algorithm

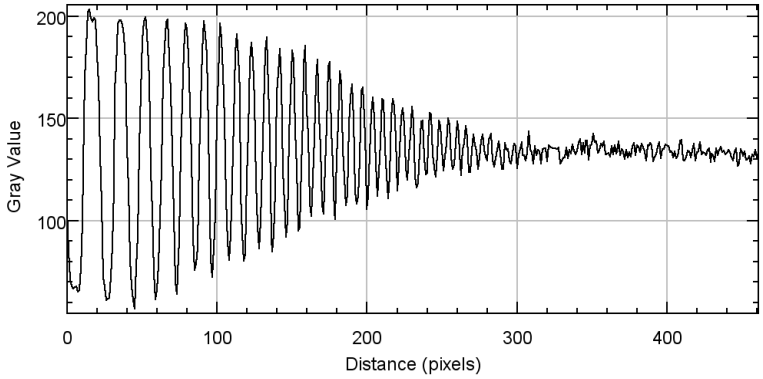

b. Line profile for super resolution image

Figure 5.28 Super resolution result by our method

5.5.3 Reconstruction through a microscopic device

To quantify the results achieved from the device, we look at the features in the image to see observable minimum distance. WBC contains minute features such as nucleus which is important for classification. Intensity profiles of different cells are examined. In order to distinguish between noise and feature, mean of background noise is calculated. If observed peak is above two standard deviations of mean of noise then it is considered as a feature. The mean of background noise was calculated to be 170.38 and 2 standard deviations corresponded to 4.76. We compared same region of white blood cell by interpolating the low resolution image four times by bicubic interpolation with our result observed a phenomenal improvement of more than twice the minimum distance observable.

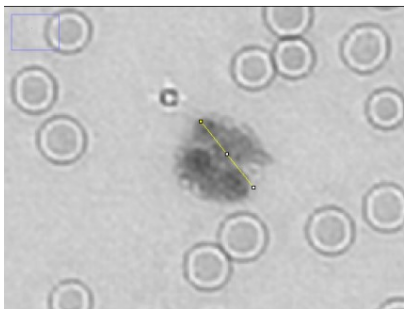

(a) Super resolution result for neutrophil WBC region

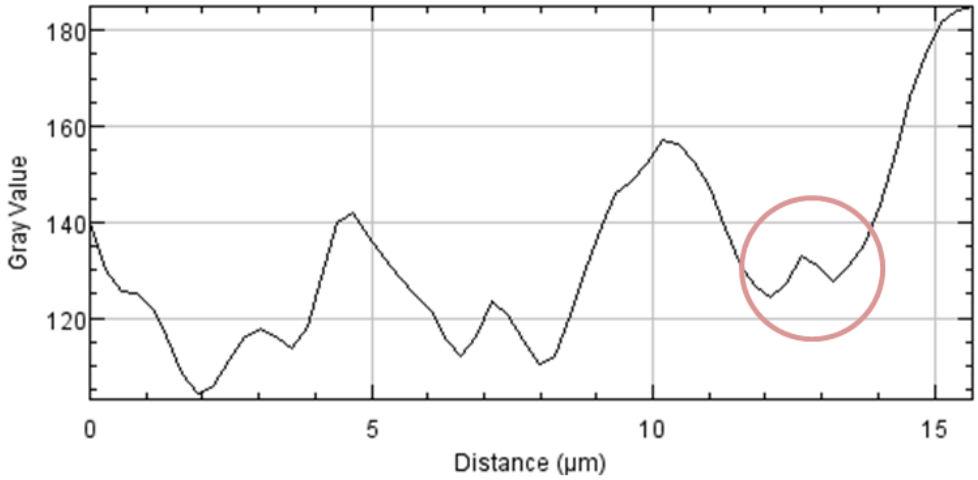

(b) Intensity profile for SR with observed peak with height of more than two standard deviations of mean of noise.

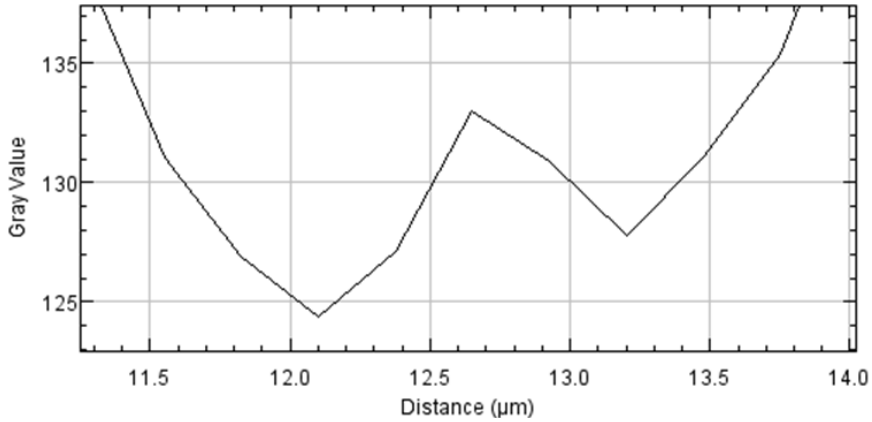

(c) Zoomed in region for the above peak; Height of the peak is 5.24µm

Figure 5.29 Minimum resolvable distance for SR

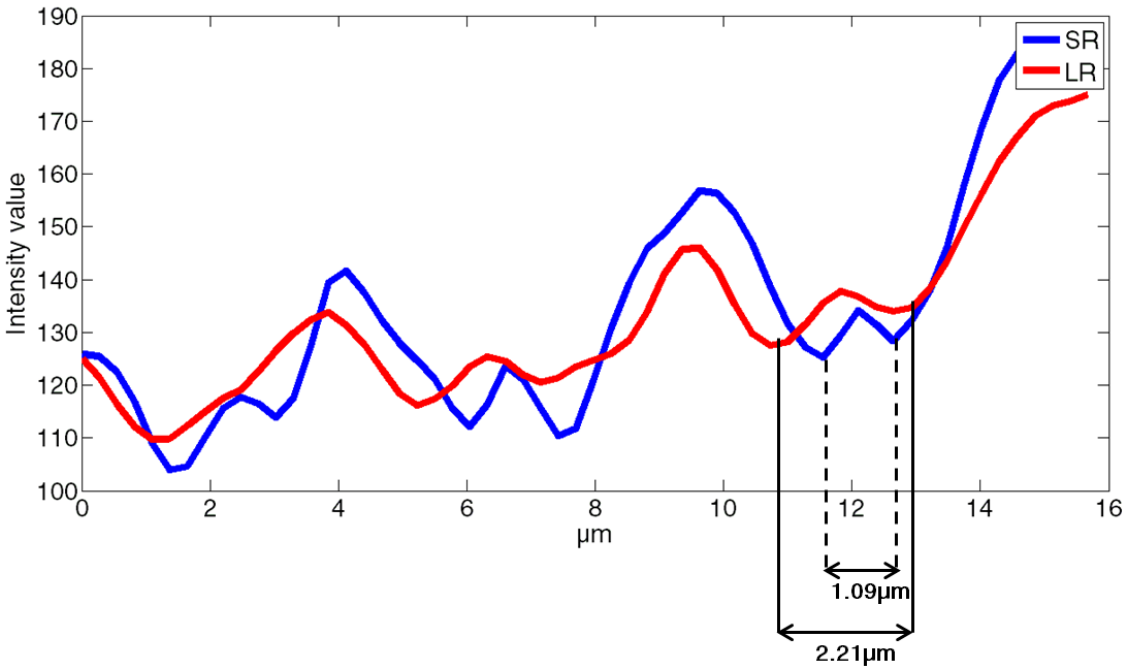

Figure 5.30 Plot comparisons between SR and LR for the same region showing minimum resolvability. Red line indicates bicubic interpolated image (4x) and blue line is our reconstruction result. Minimum distance for LR is 2.21 µm and 1.09µm for our result. Improved resolution of more than twice is observed.

Chapter 6 Conclusion and Future Work

6.1 Conclusion

We have presented a robust, computationally inexpensive super resolution algorithm that provided excellent results. Firstly, the algorithm was tested on LR dataset generated from a known ground truth image. Different images were used and combined to generate super resolved image which was compared with the original image. The images were tested with different noisy environments ranging from images captures from security cameras, to show the efficiency of our method. The results were satisfactory. Tests were carried out to generate pseudo flat field image from the on-chip system to correct the captured images and our algorithm was tested.

We improved a fast motion estimation method that searches the best location for finding subpixel shifts which is independent of the hardware configuration of the device from which microscopic images are obtained. The results were examined based on edge details, SSIM values, spatial frequency and minimum resolvable distance between features.

Sharp edges were obtained in WBC, RBC, platelets and reticulocytes which were tested by edge detection method and intensity profile. Our results were compared to other popular methods and proved to be superior with respect to details and computation time through qualitative and quantitative analysis.

Tests were carried with different experimental low resolution datasets to show the robustness of our algorithm. The improvement was measured not only through qualitative examination but also by measuring resolution in the super resolution reconstructed results. It's interesting to note that part of this work was published in [63] entitled "Measurement of Super Resolution Performance".

6.2 Suggestions for future work

This research emphasize on effectiveness of computation time in implementing the super resolution algorithm. There is always a trade-off between the higher details in reconstruction and time taken to process the whole program. Although, the achievement of quality of image is high in less time, there is still scope of improvement in the algorithm with additional consideration of some factors. Some of them are as follows:

- Incorporating sensor blur and rotation estimation within the algorithm will be useful as we concentrated on transitions which are horizontal and vertical shifts only. This would improve the accuracy of motion estimation further.
- Blur identification based on microscopic LR dataset which is challenging and computationally expensive problem.
- Modifying the algorithm for region based super resolution on different cellular structures.
- Modified median filter or advanced post processing filter which can reduce noise adapted to certain area regions in the image.
- Addition of fast deconvolution algorithm for to deblur the output image which would further enhance reconstruction result.
- Optimized method to consider best frames for super resolution.

Appendix

A.1 Derivation of Structural Similarity Index

$$SSIM(x,y) = l(x,y)^{\alpha} \cdot c(x,y)^{\beta} \cdot s(x,y)^{\gamma}$$

By setting parameters, $\alpha = 1$, $\beta = 1$, and $\gamma = 1$ and $C_3 = {}^{C_2}/_{2}$

$$SSIM(x,y) = \frac{2\mu_x\mu_y + C_1}{\mu_x^2 + \mu_y^2 + C_1} \cdot \frac{2\sigma_x\sigma_y + C_2}{\sigma_x^2 + \sigma_y^2 + C_2} \cdot \frac{\sigma_{xy} + C_3}{\sigma_x\sigma_y + C_3}$$

$$= \frac{2\mu_x\mu_y + C_1}{\mu_x^2 + \mu_y^2 + C_1} \cdot \frac{2\sigma_x\sigma_y + C_2}{\sigma_x^2 + \sigma_y^2 + C_2} \cdot \frac{\sigma_{xy} + C_2/2}{\sigma_x\sigma_y + C_2/2}$$

$$= \frac{2\mu_x\mu_y + C_1}{\mu_x^2 + \mu_y^2 + C_1} \cdot \frac{2\sigma_x\sigma_y + C_2}{\sigma_x^2 + \sigma_y^2 + C_2} \cdot \frac{2\sigma_{xy} + C_2}{2\sigma_x\sigma_y + C_2}$$

$$= \frac{(2\mu_x\mu_y + C_1)}{(\mu_x^2 + \mu_y^2 + C_1)} \frac{(2\sigma_{xy} + C_2)}{(\sigma_x^2 + \sigma_y^2 + C_2)}$$

For, $C_1 = C_2 = 0$,

$$SSIM(x,y) = \frac{(2\mu_x\mu_y)}{(\mu_x^2 + \mu_y^2)} \frac{(2\sigma_{xy})}{(\sigma_x^2 + \sigma_y^2)}$$

Bibliography

[1] Rolf T. Borlinghaus, Super-Resolution – On a Heuristic Point of View About the Resolution of a Light Microscope

[2] W. Lukosz, "Optical Systems with Resolving Powers Exceeding the Classical Limit*," J. Opt. Soc. Am. 56, 1463-1471 (1966)

[3] S. Farsiu , M. D. Robinson , M. Elad and P. Milanfar "Fast and robust multiframe super-resolution", IEEE Trans. Image Process., vol. 13, no. 10, pp.1327 -1344 2004

[4] T. Q. Pham , L. J. v. Vliet and K. Schutte "Robust fusion of irregularly sampled data using adaptive normalized convolution", EURASIP J. Appl. Signal Process., 2006

[5] Glasner, D., Bagon, S., Irani, M.: Super-Resolution from a Single Image. In: International Conference on Computer Vision, ICCV (October 2009)

[6] Yushuang Tian; Kim-Hui Yap, "Joint Image Registration and Super-Resolution From Low-Resolution Images With Zooming Motion," in Circuits and Systems for Video Technology, IEEE Transactions on , vol.23, no.7, pp.1224-1234, July 2013

[7] S.C. Park, M. K. Park, and M. G. Kang, "Super-resolution image reconstruction: a technical overview," IEEE Signal Processing Magazine, vol. 20, no. 3, pp. 21-36, 2003.

[8] Super Resolution of Images and Video, Morgan and Claypool, 2007

[9] R. Y. Tsai and T. S. Huang, "Multiframe image restoration and registration," *Adv.Comput. Vis. Image Process.*, vol. 1, pp. 317–339, 1984.

[10] B. C. Tom, N. P. Galatsanos, and A. K. Katsaggelos, "Reconstruction of a high resolution image from multiple low resolution images," in *Super-Resolution Imaging*, Chap. 4, S. Chaudhuri, Ed. Kluwer Academic Publishers, Boston/Dordrecht/London, 2001, pp. 73–105.

[11] P. E. Eren, M. I. Sezan, and A. M. Tekalp, "Robust, object-based high-resolution image reconstruction from low-resolution video," *IEEE Trans. Image Process.*, vol. 6, pp. 1446–1451, 1997. doi:10.1109/83.624970

[12] D. Slepian and H. Pollack, "Prolate Spheroidal wave functions, Fourier Analysis and uncertainty - I," Bell Systems Technical Journal, vol. 40, pp. 43-63, 1961.

[13] SLIDE: subspace-based line detection. Aghajan, H.K.; Kailath, T. Conference: ICASSP '93. IEEE International Conference on Acoustics, Speech and Signal Processing, 27-30 April 1993, Minneapolis, MN, USA

[14] K. Aizawa , T. Komatsu and T. Saito "Acquisition of Very High Resolution Images Using Stereo Cameras", Proc. SPIE Visual Communications and Image Processing \'91, pp.318 - 328 1991

[15] R. Y. Tsai and T. S. Huang. Multiframe image restoration and registration. In R. Y. Tsai and T. S. Huang, editors, Advances in Computer Vision and Image Processing, volume 1, pages 317–339. JAI Press Inc., 1984.

[16] S. P. Kim, N, K. Bose, and H. M. Valenzuela, "Recursive Reconstruction of High Resolution Image From Noisy Undersampled Multiframes," IEEE Trans. on Accoustics, Speech and Signal Processing^ vol. 38, no. 6, pp. 1013-1027, June 1990.

[17] K. D. Sauer, J. P. Allebach: Iterative reconstruction of band-limited images from nonuniformly spaced samples. IEEE Trans. CAS-34/12 (1987).

[18] H. Ur and D. Gross, "Improved Resolution from Sub-pixel Shifted Pictures," CVG IP'.Graphical Models and Image Processing, vol. 54, pp. 181-186, March 1992.

[19] A. Papoulis, "Generalized Sampling Theorem," IEEE Trans, on Circuits and Systems, vol. 24, pp. 652-654, November 1977.

[20] J. L. Brown, "Multi-Channel Sampling of Low Pass Signals," IEEE Trans, on Circuits and Systems, vol. CAS-28, no. 2, pp. 101-106, February 1981.

[21] M. Irani and S. Peleg, “Improving resolution by image registration,” CVGIP: Graphical Models and Image Proc., vol. 53, pp. 231-239, May 1991

[22] T. Q. Pham , L. J. v. Vliet and K. Schutte "Robust fusion of irregularly sampled data using adaptive normalized convolution", EURASIP J. Appl. Signal Process., 2006

[23] A. Zomet, A. Rav-Acha, and S. Peleg, “Robust super resolution,” in Proc. Int. Conf. Computer Vision and Patern Recognition, vol. 1, Dec. 2001, pp. 645–650.

[24] Glasner, D., Bagon, S., Irani, M.: Super-Resolution from a Single Image. In: International Conference on Computer Vision, ICCV (October 2009)

[25] H. He and W. C. Siu. Single image super-resolution using gaussian process regression. In CVPR, 2011.

[26] Deng, L.; Guo, W.; Huang, T., "Single image super-resolution via an iterative reproducing kernel Hilbert space method," in Circuits and Systems for Video Technology, IEEE Transactions on , vol.PP, no.99, pp.1-1 doi: 10.1109/TCSVT.2015.2475895

[27] W. T. Freeman , T. R. Jones and E. C. Pasztor "Example-based super-resolution", IEEE Comput. Graph. Appl., vol. 22, no. 2, pp.56 -65 2002

[28] J. Yang , J. Wright , T. Huang and Y. Ma "Image super-resolution via sparse representation", IEEE Trans. Image Process., vol. 19, no. 11, pp.2861 -2873 2010

[29] Mudenagudi, U.; Banerjee, S.; Kalra, P.K., "Space-Time Super-Resolution Using Graph-Cut Optimization," in Pattern Analysis and Machine Intelligence, IEEE Transactions on , vol.33, no.5, pp.995-1008, May 2011 doi: 10.1109/TPAMI.2010.167

[30] B. K. Gunturk, Y. Altunbasak, and R. Mersereau, "Bayesian Resolution Enhancement Framework for Transform-Coded Video," in Proc. IEEE Int. Conf. on Image Processing, Thessaloniki, Greece, 2001, pp. 41-44.

[31] Abbe, E. (1873). "Beitrage zur Theorie des Mikroskops und der mikroskopischen Wahrmehmung". Archiv für Mikroskopische Anatomie 9: 413–420. doi:10.1007/BF02956173.

[32] Michael W. Davidson. "Resolution." ZEISS Microscopy Online Campus. Carl Zeiss Microscopy, LLC, United States, n.d. Web. 18 Dec 2015

[33] *A. Cornea, P. Michael Conn*, Fluorescence Microscopy Super-Resolution and other Novel Techniques

[34] Psf analysis and image deblurring using a simulated camera lens - Teach. (n.d.). Retrieved from http://white.stanford.edu/teach/index.php/Psf_analysis_and_image_deblurring_using_a_simulated_camera_lens

[35] Nikon MicroscopyU | Modulation Transfer Function. (n.d.). Retrieved from https://www.microscopyu.com/articles/optics/mtfintro.html Anil K. Jain, Fundamentals of Digital Image Processing. Prentice Hall, 1989.

[36] R. Boyle and R. Thomas Computer Vision: A First Course, Blackwell Scientific Publications, 1988, pp 32 - 34.

[37] B. Girod, “What’s wrong with mean-squared error,” in Digital Images and Human Vision (A. B. Watson, ed.), pp. 207–220, the MIT press, 1993.

[38] P. C. Teo and D. J. Heeger, “Perceptual image distortion,” in Proc. SPIE, vol. 2179, pp. 127–141, 1994.

[39] A. M. Eskicioglu and P. S. Fisher, “Image quality measures and their performance,” IEEE Trans. Communications, vol. 43, pp. 2959–2965, Dec. 1995.

[40] Z. Wang, A. C. Bovik, and L. Lu, “Why is image quality assessment so difficult,” in Proc. IEEE Int. Conf. Acoust., Speech, and Signal Processing, vol. 4, (Orlando), pp. 3313–3316, May 2002.

[41] Z. Wang, A. C. Bovik, H. R. Sheikh, and E. P. Simoncelli, , "Image quality assessment: From error measurement to structural similarity" , *IEEE Trans. Image Process.* , vol. 13 , no. 4 , pp.600 -612 , 2004

[42] N. Senthilkumaran1, R. Rajesh Edge detection techniques for image segmentation-a survey of soft computing approaches International Journal of Recent Trends in Engineering, 1 (2) (2009), pp. 250–254

[43] Bo Peng, Lei Zhang, David Zhang, A survey of graph theoretical approaches to image segmentation, Pattern Recognition, Volume 46, Issue 3, March 2013, Pages 1020-1038, ISSN 0031-3203, http://dx.doi.org/10.1016/j.patcog.2012.09.015.

[44] R.C. Gonzalez, R.E. Woods, Digital Image Processing Addison Wesley, Reading, MA (1992)

[45] J. Canny.A computational approach to edge detection IEEE Trans. Pattern Analysis and Machine Intelligence, 8 (1986), pp. 679–698

[46] J. Zhang and G. G. Hanauer, , "The application of mean field theory to image motion estimation" , IEEE Trans. Imag. Processing , pp.19 -33 , 1995

[47] SIPI Image Database - Misc. (n.d.). Retrieved from http://sipi.usc.edu/database/database.php?volume=misc

[48] Datasets (n.d.). Retrieved from www.computervisiononline.com/datasets

[49] B. D. Lucas and T. Kanade, , "An iterative image registration technique with an application to stereo vision" , *Proc. Int. Joint Conf. on Artificial Intelligence* , pp.674 -679 , 1981

[50] J. Y. Bouguet , *Pyramidal Implementation of the Lucas-Kanade Feature Tracker, Tech. Rep.,*, 1999

[51] B. K. P. Horn and B. G. Schunck , "Determining optical flow" , *Artif. Intell.* , vol. 17 , pp.185 -203 , 1981

[52] D. J. Fleet and Y. Weiss. Optical flow estimation. In N. Paragios, Y. Chen, and O. Faugeras, editors, Handbook of Mathematical Models in Computer Vision, chapter15, pages 239–258. Springer, 2006.

[53] Williams, Timothy C. and Shaddix, Christopher R., Review of Scientific Instruments, 78, 123702 (2007), DOI:http://dx.doi.org/10.1063/1.2821616

[54] Milanfar, P. (n.d.). Multi-Dimensional Signal Processing Research Group Super-Resolution And Demosaicing Datasets. Retrieved from www.soe.ucsc.edu/~milanfar/software/sr-datasets.html

[55] Samson, E. C., & Blanca, C. M. (2007). Dynamic contrast enhancement in widefield microscopy using projector-generated illumination patterns. New Journal of Physics, 9(10), 363.

[56] Kang, Y.U.; Jeong, S.-C.; Song, B.C., "Fast super-resolution algorithms using one-dimensional patch-based training and directional interpolation," in *Image Processing, IET* , vol.6, no.5, pp.548-557, July 2012

[57] Timofte, R.; De, V.; Van Gool, L., "Anchored Neighborhood Regression for Fast Example-Based Super-Resolution," in *Computer Vision (ICCV), 2013 IEEE International Conference on* , vol., no., pp.1920-1927, 1-8 Dec. 2013

[58] Yu, J. Y., Holland, D. B., Blake, G. A., & Guo, C. L. (2013). The wide-field optical sectioning of microlens array and structured illumination-based planeprojection multiphoton microscopy. Optics express, 21(2), 2097-2109. 106

[59] Chowdhury, S., & Izatt, J. (2013). Structured illumination quantitative phase microscopy for enhanced resolution amplitude and phase imaging. Biomedical optics express, 4(10), 1795-1805.

[60] Junjun Jiang; Xiang Ma; Zhihua Cai; Ruimin Hu, "Sparse Support Regression for Image Super-Resolution," in *Photonics Journal, IEEE* , vol.7, no.5, pp.1-11, Oct. 2015

[61] IEEE Standard on Video Techniques: Measurement of Resolution of Camera Systems, 1993 Techniques," in IEEE Std 208-1995 , vol., no., pp.0_1-, 1995

[62] Test TARGETS & CHARTS. (n.d.). Retrieved from https://www.appliedimage.com/products/test-targets-and-charts-1

[63] R. Kainth, A. Fine, M. Cada, “Measurement of Super Resolution Performance,” *Photonics North, 2016*, Quebec City, QC, 2016